



Stockholm
University

Master Thesis

Degree Project in
Marine Geology 60 hp

Hydroclimatic variations over the past ~17,400 years in the Lesotho Highlands, southern Africa: a geochemical proxy approach

Mikaela Holm



Stockholm 2017

Department of Geological Sciences
Stockholm University
SE-106 91 Stockholm

Abstract

Southern Africa is considered one of the most climate sensitive regions in the world. Slight variations in ocean temperatures and pressure systems regularly lead to droughts or flooding. Such water stress, in combination with poor climate adaptation, may have devastating consequences, particularly given that most people in the region are dependent on subsistence agriculture. A better understanding of the complex mechanisms driving hydrological variability can be gained by studying proxies linked to changes in climate in the past.

Previous work by Fitchett et al. (2016b) used fossil pollen and diatom data together with sedimentological data to reconstruct past variations in vegetation, relative temperatures as well as wetland water tables over the last ~16,000 cal. BP in the Sekhokong Mountain Range, in Lesotho. New continuous high-resolution samples that span the period from 17,335 to 13,440 cal. BP are used to extend and augment the resolution of the previously studied sequence. Conventional XRF, FTIR-ATR, C/N and stable carbon isotope methods are used on this new sequence as well as to compliment the original dataset, revealing details of paleo-earth processes including weathering, sediment movement and transport, biological productivity, degradation and changes in material sources. Based on the geochemical proxies, constructed from two independent, but agreeing, geochemical datasets, five units representing the major hydroclimatic shifts were identified. The proxy data indicate relatively wet conditions during Unit D (17,335 to 16,115 cal. BP). This is followed by Unit C, which was a period of drier conditions (16,115 to 15,315 cal. BP). A rapid moisture increase occurs in Unit B with relatively wet conditions (15,315 to 14,175 cal. BP). Unit A (14,175 to 13,440 cal. BP) reveals multiple fluctuations between relatively dry conditions and relatively wet conditions. In Unit 1, covering 13,280 cal. BP to present, the geochemical proxies suggest relatively wet conditions with a few drier intervals occurring between 8,560 cal. BP to 6,970 cal. BP, at 5,520 cal. BP, 3,300 cal. BP and after 1,110 cal. BP.

Based on comparisons between multiple records, drier periods in the Lesotho Highlands occur during colder conditions in the southern Hemisphere. Likely as a consequence of a northward extension of the polar vortex and migration of the ITCZ, which strengthened the influence of the westerlies and changed the source of moisture from the east (Indian Ocean) to the west (Atlantic Ocean). During warmer periods and increased sea surface temperature (SST) in the Indian ocean, the local hydrological conditions tend to be relatively wet in the Sekhokong area. This suggests an association between higher SSTs in the Indian Ocean and increased rainfall in southeastern Africa.

When multiple proxies are used in parallel, it is possible to distinguish between various climate forced processes, which is important for establishing large-scale migrations of circulation systems and the controlling mechanisms. This study spans from the Late Glacial to present, a period for which the paleoclimate is not yet resolved for southern Africa, addressing an important gap in this climate data-poor region.

Table of Contents

Abstract	2
1. Introduction	6
<i>Aim</i>	7
2. Background	7
2.1. <i>Hydrology controlling climate systems in southern Africa</i>	7
2.2. <i>Previous environmental reconstructions in southern Africa</i>	9
2.2.1. Last glacial maximum	9
2.2.2. Deglaciation	10
2.2.3. Younger Dryas	11
2.2.4. Holocene	11
2.3. <i>Geochemistry and paleoclimatology</i>	12
3. Study area	14
4. Materials and methods	15
4.1. <i>Radio carbon dating and age model construction</i>	17
4.2. <i>Carbon, nitrogen and stable carbon isotope analysis</i>	18
4.3. <i>XRF analysis</i>	18
4.4. <i>FTIR-ATR analysis</i>	19
4.5. <i>XRD analysis</i>	19
4.6. <i>Biogenic silica extraction and identification</i>	19
4.7. <i>Statistical analysis</i>	20
4.7.1. FTIR-ATR data	20
4.7.2. Elemental geochemistry data	20
5. Results	21
5.1. <i>SEK2014</i>	21
5.1.1. Organic chemistry: TOC, C/N ratios and $\delta^{13}\text{C}$	23
5.1.2. FTIR-ATR PCA	23
5.1.3. Elemental PCA	24
5.1.4. Si/Ti ratio	24
5.2. <i>SEK2016</i>	25
5.2.1. Organic chemistry: TOC, C/N ratios and $\delta^{13}\text{C}$	26
5.2.2. FTIR-ATR PCA	29
5.2.3. Elemental PCA	31
5.2.4. Si/Ti ratios	32
5.2.5. XRD	32
5.2.6. Biogenic silica	34
6. Discussion	35
6.1 <i>Extraction of significant factors</i>	35
6.2 <i>Interpreting the proxies</i>	36
6.3 <i>Paleohydroclimatic interpretation</i>	39
6.3.1. SEK2016 Unit D: 17,335 to 16,115 cal. BP	39
6.3.2. SEK2016 Unit C: 16,115 to 15,315 cal. BP	39
6.3.3. SEK2016 Unit B: 15,315 to 14,175 cal. BP	40
6.3.4. SEK2016 Unit A: 14,175 to 13,440 cal. BP	41
6.3.5. SEK2014 Unit 1: 13,280 cal. BP to present	41
6.4 <i>Regional context and implication of forcing mechanisms</i>	43
7. Conclusions	48
Acknowledgments	49
References	50

Appendix A, Age-depth model	57
Appendix B, Linear regression models	58
Appendix C, Conventional XRF	62
Appendix D, XRD	63

1. Introduction

According to the IPCC climate change will have a major effect on the hydrological cycle of southern Africa, due to shifts in temperature and rain patterns, impacting the already stressed water resources as a consequence (Boko et al., 2007; Niang et al., 2014). This is particularly important in light of the fact that a majority of the people in the region are dependent on subsistence agriculture and the utilization of land-based resources such as lakes and rivers (Olago and Odada, 2004; Reason et al., 2006). Since the water-bearing weather systems are altered by topographical variations, high altitude areas such as the eastern Lesotho escarpment works as a “water tower” for the surrounding areas (Gasse and Battarbee, 2004). This makes Lesotho one of the main water resources for the Johannesburg area (Grab and Deschamps, 2004) in the Gauteng province, with a population of almost 12.3 million (STATSSA, 2017). In order to better predict how future climate change will impact this water resource we must understand the underlying mechanisms controlling the hydrological system in the region. This can be done by looking at paleoclimatic archives and environmental proxies (Baker et al., 2017).

Insight into past environmental changes in eastern Lesotho was gained in a study by Fitchett et al. (2016b), which was based on fossil pollen and diatoms from the Sekhokong Mountain Range. This study by Fitchett et al. (2016b) was however based on discrete samples covering the period from 16,450 cal. BP to present, with important information about the deglaciation missing. This study extends and augments the resolution of the sequence studied by Fitchett et al. (2016b). We work to improve our understanding of these changes by performing geochemical analyses on both the original Sekhokong sample set as well as new, high-resolution samples. The latter span the period from 17,335 to 13,440 cal. BP, which covers much of the last glacial-interglacial transition (18,000 to 11,700 cal. BP; Valsecchi et al., 2013). By introducing geochemical data, namely total organic carbon (TOC), stable carbon isotope data ($\delta^{13}\text{C}$), carbon/nitrogen ratio (C/N ratio), Fourier transform infrared spectroscopy attenuated total reflectance (FTIR-ATR) and X-ray fluorescence (XRF) elemental data, paleoclimatic variations over time can be better understood. These proxies can trace geochemical signals as expressed through weathering, sediment movement and transport, biological productivity, degradation and changes of material sources – processes all controlled by the hydrological regime (Oldfield and Thompson, 2004). Variations in these processes are strongly linked to climate change, forced by underlying mechanisms that control large-scale migrations of circulation systems (Meyers, 2003). Its age, continuity and resolution make the Sekhokong record unique in southern Africa.

Aim

The aim of this project is to reconstruct paleohydrological changes in the Lesotho Highlands from 17,335 cal. BP to present. The specific objectives are to:

- Identify processes controlling the geochemical signature of the studied sediment sequence
- Reconstruct the paleohydrological conditions over the last 17,335 cal. BP, with specific focus on 17,335 to 13,440 cal. BP
- Connect the identified paleohydrological variations to large-scale climate forcing and mechanisms

2. Background

2.1. Hydrology controlling climate systems in southern Africa

The systems controlling the climate and weather in southern Africa are complex. Located in the subtropics, this region is influenced by tropical circulation systems in the north and temperate circulation systems in the south (Tyson and Preston-Whyte, 2000). Based on annual variations in rain distribution, southern Africa can be divided into three zones (Figure 1): the Winter Rainfall Zone (WRZ), the Year-Round Rainfall Zone (YRZ) and the Summer Rainfall Zone (SRZ) (Reason et al., 2006). During the summer (October to March) insolation is stronger, which increases the heating of the land areas, and a near-surface low pressure is formed over the continent (Schefuß et al., 2011; Tyson and Preston-Whyte, 2000). This low pressure increases the moisture transport to the continent from the surrounding oceans. The Inter-Tropical Convergence Zone (ITCZ) migrates from the northern hemisphere (15 to 18° N) to the southern hemisphere (5 to 6° S in western Africa and 15 to 20° S in eastern Africa), which shifts the atmospheric circulation systems southward (Tyson and Preston-Whyte, 2000). The influence of the easterlies over southern Africa increases as the atmospheric circulation migrates. Moist air from the Indian Ocean is transported by the easterlies over the southern African subcontinent, resulting in increased rainfall in the SRZ. Cloud-band formation over the Indian Ocean, which is a summer phenomenon, is one of the most important moisture sources in the SRZ (Reason et al., 2006; Tyson and Preston-Whyte, 2000).

The margin between the Atlantic and the Indian Ocean airstreams forms the Congo Air Boundary (CAB), which migrates during the year and influences moisture transport and the geographical distribution of rainfall (Gasse et al., 2008). During the austral winter (April to September) a high pressure forms over southern Africa and the ITCZ migrates to the northern hemisphere, which pushes the position of the atmospheric circulation systems northwards (Schefuß et al., 2011; Tyson and Preston-Whyte, 2000). The influence of the westerlies increases as they move towards the equator and bring moisture from the South Atlantic Ocean to the WRZ and the YRZ (Chase and Meadows, 2007).

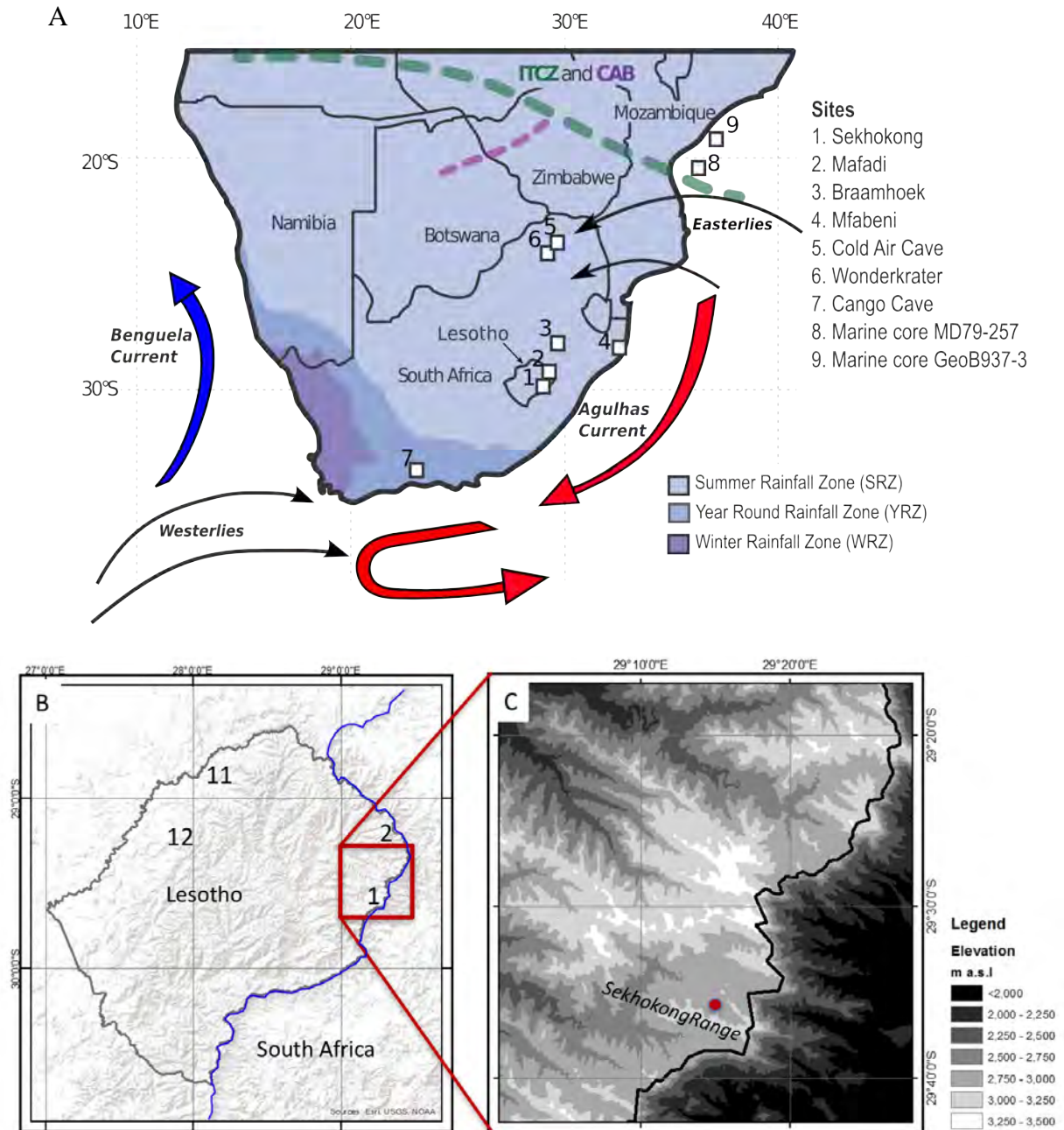


Figure 1. (A) shows southern Africa with the Atlantic Ocean to the west and the Indian Ocean to the east. The different rainfall zones are marked out as well as the location of the main studies discussed in this report. The figure also presents some of the atmospheric and oceanic circulation patterns, the Inter-Tropical Convergence Zone (ITCZ) and the Congo Air Boundary (CAB) that are controlling the climate in the SRZ. (B) shows the Lesotho boarder (grey line), the Drakensberg escarpment (blue line) and four study sites discussed in this report: (1) Sekhokong, which includes this study, Marker (1994) and Fitchett et al. (2016b), (2) Mafadi wetland (Fitchett et al., 2016c), (11) Ha Makotoko and Ntloana, two archaeological sites (Roberts et al., 2013) and (12) Archaeological sites within the Caledon River Valley (Smith et al., 2002). The terrain model source: ESRI, USGS and NOAA (ESRI et al., 2009). (C) shows the elevation around the Sekhokong Range. The sampling site is marked out with a red dot. The elevation data is from ASTER GDEM, which is a product of METI and NASA (USGS, 2017)

The SST of the surrounding oceans has an important control on convection and moisture fluxes (Tyson and Preston-Whyte, 2000). The cold Benguela Current along the southern African west coast has an effect on the regional climate, with decreased rainfall in the WRZ due to reduced vapour flux (Stone, 2014). The Agulhas Current, mainly supplied by warm water from a South-West Indian Ocean recirculation gyre driven by the South Indian anticyclone (Tyson and Preston-Whyte, 2000), increases the moisture flux in the SRZ (Stone, 2014).

The rain distribution in southern Africa is also controlled by topographic differences due to the Drakensberg escarpment (Sene et al., 1998) (Figure 1B). Areas near the escarpment, such as the eastern Lesotho boarder, receive more rain than areas further to the west as a result of orographic effects (Norström et al., 2009).

2.2. Previous environmental reconstructions in southern Africa

There is a lack of long-term terrestrial environmental reconstructions from southern Africa, especially considering continuous high-resolution archives, and what is available has an uneven geographical distribution (Gasse et al., 2008; Scott and Lee-thorp, 2004; Truc et al., 2013). The lack of continuous lake records and other organic rich archives is a consequence of several factors including the geological setting and repeated evaporation and desiccation cycles that break down organic matter (OM) (Scott and Lee-thorp, 2004). It is therefore very important to increase the number of paleoclimatic studies in southern Africa, such as this hydroclimatic reconstruction from the Sekhokong.

The connection between climatic variations, revealed from paleoenvironmental studies in southern Africa, and controlling mechanisms are not fully understood (Norström et al., 2009). However, cyclic variations in insolation due to Earth's orbital geometry are believed to be a major external forcing mechanism affecting the global climate system (Berger, 1978; Laskar et al., 2004). These insolation variations influence the atmospheric circulation systems and the latitudinal position of the ITCZ, which is believed to be one of the major paleoclimate forcings in southern Africa (Schefuß et al., 2011; Truc et al., 2013).

2.2.1. Last glacial maximum

The last glacial maximum (LGM, 21,000 cal. BP; Chevalier et al., 2017) is thought to have been a cold period in southern Africa as seen in a number of different studies (Baker et al., 2017; Finch and Hill, 2008; Grab, 2002; Holmgren et al., 2003; Partridge et al., 2004). Speleothem analysis from Cango Cave in the southern part of South Africa indicate conditions with temperatures 5-6° C colder during the LGM as compared with today (Partridge et al., 2004). Terrestrial archives from the Mfabeni Wetland in the eastern African sub-tropics, indicate drier conditions (Baker et al., 2017; Finch and Hill, 2008) and the majority of southern Africa's lake levels lowered during the LGM, with some drying out (Partridge et al., 2004). A study by Sonzogni et al. (1998) reconstructing SST derived from alkenones from 18 marine sediment cores, including MD79-257 (discussed later), shows colder conditions during the late glacial.

2.2.2. Deglaciation

During the Pleistocene – Holocene transition, the climate changes from cold and dry LGM conditions to warmer Holocene conditions (Fitchett et al., 2016b; Holmgren et al., 2003). However, this transition is suggested to have been very unstable with multiple rapid shifts in temperature and humidity, based on C₃ and C₄ shifts in the Lesotho lowland (Smith et al., 2002) and $\delta^{13}\text{C}$ and $\delta^{18}\text{O}$ records of ungulate grazers from archaeological sites in Lesotho (Roberts et al., 2013). During deglaciation, southeastern Africa became warmer and more humid (Gasse and Battarbee, 2004). One of the main reasons for the increased moisture during deglaciation is believed to be due to raised SSTs in the western Indian Ocean (Truc et al., 2013). Increased SST may result in increased heat budget to water-bearing weather systems (Partridge et al., 2004). The major forcing mechanism suggested to have controlled the Indian Ocean SSTs and strengthening of the warm Agulhas current is linked to changes within the Antarctic circumpolar vortex (Partridge et al., 2004).

In a study by Baker et al. (2017) the depositional environment at the Mfabeni wetland, in eastern South Africa, was reconstructed using TOC and $\delta^{13}\text{C}$ values both of the bulk and leaf wax. The main focus was to establish shifts between terrestrial C₃ and C₄ plants as a response to changes in temperature and precipitation patterns, which suggested cold and dry conditions during the LGM until c. 15,000 cal. BP. This is followed by a rapid change to more humid conditions indicated by a significant increase in TOC values (Baker et al., 2017, 2014). Fitchett et al. (2016b) suggest wetland enlargement after 16,450 cal. BP. This wet period lasted until 14,440 cal. BP, but was interrupted by very dry conditions during 16,350-15,870 cal. BP. Holmgren et al. (2003) suggest that the post-glacial warming inferred from Cold Air Cave $\delta^{18}\text{O}$ stalagmite record started 17,500 cal. BP with a cold period between 15,000-13,500 cal. BP; this was proposed to be a response to the Antarctic Cold Reversal (ACR). The ACR is well documented by changes in $\delta^{18}\text{O}$ in Antarctic ice cores, which indicates an abrupt cooling during 14,000 to 12,500 cal. BP (Jouzel et al., 2001). A northward extension of the Antarctic convergence, as a consequence of the ACR, increased the strength and influence of the westerlies, resulting in decreased rainfall in the SRZ (Partridge et al., 2004).

The same relative changes, with a colder period before warmer and wetter conditions from 13,500 to 9,000 cal. BP is suggested by Marker (1994), in an environmental reconstruction from Lesotho Highlands. The study was based on sedimentological proxies on low-resolution discrete samples obtained from seven sediment sequences in the Sekhokong Mountain Range. A return to drier conditions in the Sekhokong Mountain Range area at 14,150 cal. BP is inferred by relative pollen data, increased sand-particles and increased carbonates, after which the system successively became warmer and wetter over time (Fitchett et al., 2016b).

2.2.3. Younger Dryas

The Northern hemisphere underwent a glacial re-advance, referred to as the Younger Dryas (YD), which lasted for a short period between 12,900-11,600 cal. BP (Bond and Lotti, 1995; Grootes et al., 1993). Like the Heinrich events, YD have been well recorded in North Atlantic sediments and in Greenland ice cores (Bond and Lotti, 1995; Grootes et al., 1993). Whether or not the forcing mechanisms causing the YD, also affected the climate in southern Africa, or the southern hemisphere in general, is not yet resolved (Gasse et al., 2008). Dry conditions in eastern parts of southern Africa corresponding to the timing of YD are suggested by a hiatus in speleothems records from Cold Air Cave (Holmgren et al., 2003) and Cango Cave (Talma and Vogel, 1992), pollen data from Wonderkrater (Truc et al., 2013) as well as pollen and diatom records (Norström et al., 2009) and biomarkers and geochemical proxies (Norström et al., 2014) from the Braamhoek wetland.

Geochemical and geophysical data, such as $\delta^{18}\text{O}$, aerosol loading and snow accumulation rate, from the Taylor Dome ice core (Antarctica) show synchronous, or near- synchronous, trends compared to the central Greenland ice cores as well as other North Atlantic archives (Steig et al., 2000). Other studies have shown an antiphase response between climatic events in the northern hemisphere and the southern hemisphere (Baker et al., 2017; Chase et al., 2015; Pedro et al., 2011). The inter-hemispheric coupling, whether it is synchronic or out-of-phase and the oceanic and atmospheric integration, is not fully understood.

2.2.4. Holocene

The environmental reconstruction by Truc et al. (2013) from Wonderkrater suggests a general warming accompanied by more humid conditions during the early to mid-Holocene, with maximum temperatures (both summer and winter) proposed between 8,300 to 6,500 cal. BP. The Cold Air Cave $\delta^{18}\text{O}$ stalagmite record agrees with this and suggests warm conditions from 10,000 to 6,000 cal. BP (Holmgren et al., 2003). Relatively humid conditions during the early Holocene are also indicated by biomarkers at Mfabeni wetland, with a short dry event identified by low TOC at approximately 7,100 cal. BP (Baker et al., 2017). The Sekhokong Mountain Range pollen and diatom record suggests warm and gradually wetter conditions during the early Holocene, with maximum temperatures between 8,560 to 7,280 cal. BP (Fitchett et al., 2016b). However, dry and cold conditions are suggested by fossil pollen and organic geochemical proxies at Braamhoek from 9,500 to 8,500 cal. BP (Norström et al., 2009). Marker (1994) also suggest cold and possibly dry conditions in the Lesotho Highlands, from 9,000 to 5,000 cal. BP. A general temperature decline is proposed for eastern parts of southern Africa after 6,500 cal. BP, with multiple variations that last until present (Holmgren et al., 2003; Truc et al., 2013). Parker et al. (2011) suggest cooler and wetter conditions in Lesotho during 3,000 to 2,200 cal. BP followed by drier conditions, based on migration of C_3 plants to lower altitudes. Marker (1994) suggest wetter conditions from 5,000 to 1,000 cal. BP, followed by drier conditions until present times, in the Lesotho Highlands.

2.3. Geochemistry and paleoclimatology

The use of geochemical parameters in the paleolimnological research field was introduced by Mackereth in the 1960's (Boyle, 2001). Since then it has become a very important tool when reconstructing paleoenvironmental conditions using lake and wetland sediment archives. One of the main advantages when using geochemical proxies is the possibility of getting high-resolution continuous data in a more economical and efficient way compared with the more traditional biological methods, such as pollen and diatom analysis (Boyle, 2001). By understanding the behaviour of chemical substances and their paths in natural systems, important processes within the lake and catchment can be identified from chemical signatures in the sediment, and be linked to environmental change over time. The main goal is to establish the relationship between the components and the geochemical signatures in the sediment to the processes forming or transporting the material in or to the deposit, which can then be linked to larger climate controlling mechanisms (Boyle, 2001; Davies et al., 2015).

Elemental data from XRF analysis can be used to understand past changes in catchment dynamics such as variations in weathering rates, run-off intensity and erosion as well as biological productivity (Davies et al., 2015). Minerals can be identified due to differences in chemical composition, which can indicate variations in detrital input, weathering and autochthonous mineral precipitation processes. Elements such as Fe and Mn are sensitive to changes in redox conditions, and are soluble in reducing environments (Boyle, 2001). Thus, variations in Fe and Mn can be used as proxies for redox conditions, which is controlled by a number of factors such as water table levels and stratification, biological productivity and temperature (Davies et al., 2015). Using FTIR-ATR different components can be identified on the basis of their molecular structure, bond angle and length as well as the bond vibration, which results in various interaction with radiation and absorption of different wave-lengths (Swann and Patwardhan, 2011). The absorption pattern of a wavelength spectrum (in this case between 4000-400 cm^{-1}) can therefore be used to identify specific compounds (e.g., clay minerals, carbonates, biogenic silica (BSi) and OM).

The amount of OM preserved in sediments is a result of several processes: terrestrial and aquatic biological productivity, transport in the catchment and/or within the aquatic system and rate of degradation (Meyers and Teranes, 2001). The concentration of OM is also affected by the amount of inorganic matter (IM) deposited and autochthonously precipitated compounds, which dilute the OM, or dissolution of minerals which has a concentrating effect (Meyers and Teranes, 2001). The chemical composition of a plant (which makes up the largest part of sedimentary OM) varies depending on the type, whether it is vascular or non-vascular and if it is a C_3 or C_4 plant. Non-vascular plants, such as phytoplankton, generally produce OM with a C/N ratio between 4-10 (Meyers and Teranes, 2001). Vascular plants produce OM with a C/N ratio >20 due to its structure with high cellulose and lignin and low protein content (Meyers and Teranes, 2001). The C_3 or C_4 plants can be distinguished depending on their differences in carbon fractionation (Meyers, 2003). As a result of different pathways of carbon fixation, C_3 plant OM have a $\delta^{13}\text{C}$ value between -34 to -23 ‰ and C_4 plant OM have a $\delta^{13}\text{C}$ value between -9 and -17 ‰ (Smith and Epstein, 1971).

BSi can be used as a paleoenvironmental indicator of biological productivity (Conley, 1998) since it usually represents the production of diatoms (Ragueneau et al., 1996). Diatoms are siliceous phytoplankton, and therefore BSi, only captures a part of the biological productivity (Boyle, 2001; Ragueneau et al., 1996). This method must therefore be combined with other proxies that strengthen the interpretation of BSi variations as a proxy of productivity. BSi can dissolve as a result of increasing pH, leading to a geochemical signal representing dissolution rather than the decreasing productivity at the time of deposition (Boyle, 2001). It is also important to be aware of possible minerogenic contribution causing dilution effects (Takano et al., 2012).

3. Study area

The study site is located at 29°36'31" S, 29°15'54" E, in the Sekhokong Mountain Range, eastern Lesotho (Figure 1). The area is situated at approximately 2,900 m a.s.l. The wetland deposit is located in an 800 m wide and 1,200 deep valley, which is one out of at least four valley heads that has been eroded in to the north-facing basaltic slope of the Sekhokong ridge (Fitchett et al., 2016a) (Figure 1C). Today a stream has eroded through the deposit forming a 5 m deep gully revealing alternating layers of organic rich silt and clay, peat, thin sand layers and some gravel. Sedimentological analysis of the deposit made by Fitchett et al. (2016b) suggests that sedimentation has been mainly uniform across the Sekhokong site. Horizontal repetitive peat layers across the deposit (Grab and Deschamps, 2004), and absence of paleo gullies and paleo channels, agrees with the sedimentological data and further supports uniform sedimentation where channelized flow was minor or non existent (Fitchett et al., 2016b). The local geology consists of a thick (~1500 m) basaltic lava cap which overlays sedimentary rocks, limiting the origin of lithogenic input to weathered basalt.

The mean temperature in the Lesotho Highlands (measured at 3,100 m a.s.l.) is 11° C in January and 0° C in July (Grab, 1999). Since Lesotho is located within the SRZ, the major part (>80%) of the annual precipitation falls as rain during the summer months (Nash and Grab, 2010), typically due to thunderstorms and instability showers (Sene et al., 1998). The rain distribution in Lesotho varies not only annually but is also unevenly distributed within the regions due to topographic variations (Sene et al., 1998). The mean annual precipitation in the Lesotho Highlands, is around 1200 mm at the Sekhokong Range and close to the escarpment edge, as a result of orographic precipitation, and decreases to 500 mm westwards (Sene et al., 1998). Winters are typically dry and cold, with approximately eight annual snow falls that accounts for less than 10% of the annual precipitation (Fitchett et al., 2016b; Nash and Grab, 2010).

The vegetation in Lesotho is to a large extent controlled by the high altitude (Parker et al., 2011) and the Sekhokong is located above the treeline (Fitchett et al., 2016b). The vegetation in the area today is predominated by meadow grasses, sedges and small shrubs (Fitchett et al., 2016b). The area is situated above the transition zone (2,100 to 2,700 m a.s.l) where dominated C₄ grasslands gradually shifts to C₃ grasses that are more tolerant to the low austral winter temperatures (Roberts et al., 2013; Smith et al., 2002).

4. Materials and methods

This study is based on two sets of samples. The first set of samples are the same as those used and described by Fitchett et al. (2016b) from the Sekhokong site. These discrete samples span from 16,450 cal. BP to present and consist of 40 samples that cover approximately 5 m sediment sequence with variable sampling resolution (from 2 cm to 43 cm between samples). These samples had already been analysed previously for fossil pollen, fossil diatoms, organic content and grain size. These samples were sent to Stockholm University from the University of the Witwatersrand, South Africa in early 2017 and will be referred to as SEK2014 (Figure 2). In 2016, a continuous sediment sequence of 1.5 m, which overlaps and extends the Fitchett et al. (2016b) study was taken. These samples will be referred to as SEK2016 and will be the major focus in this study (Figure 2).

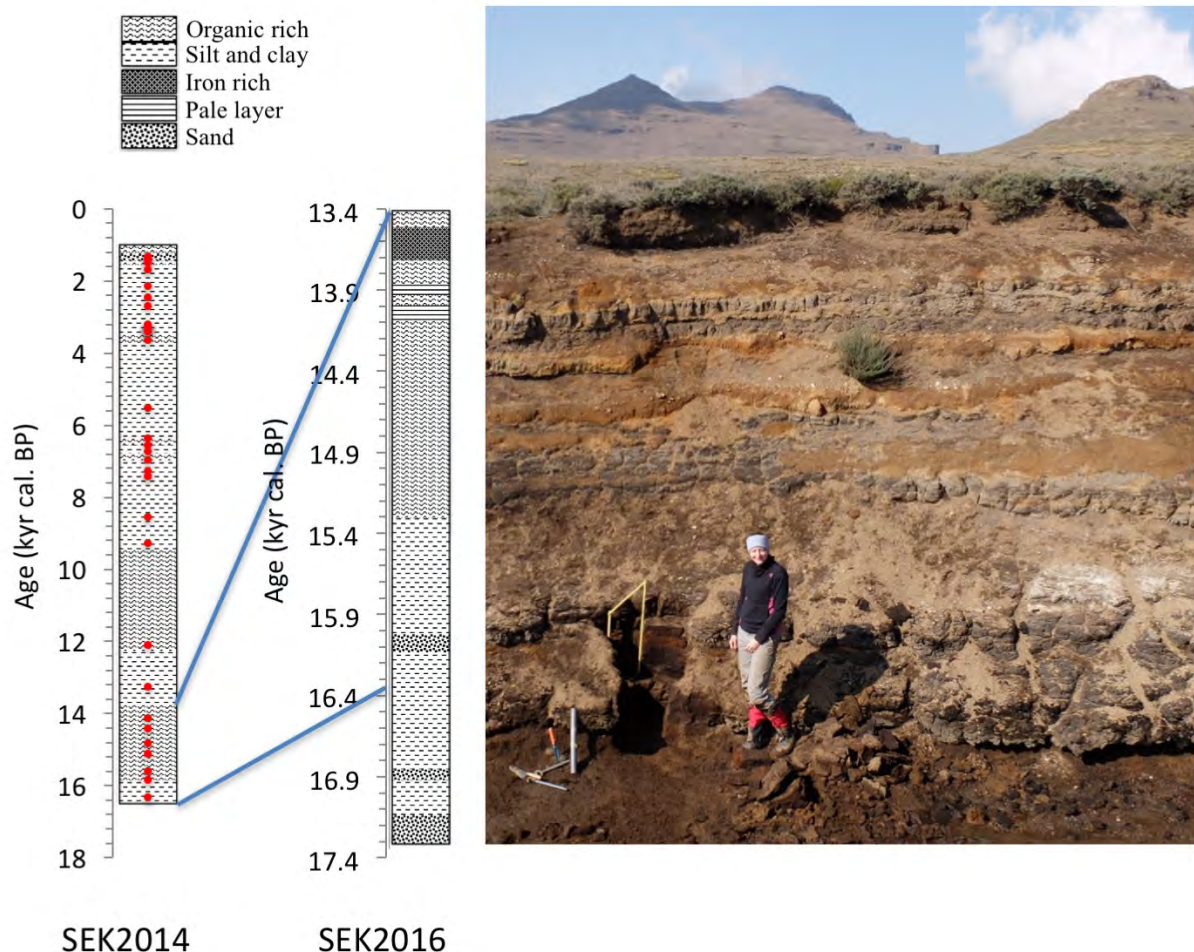


Figure 2 shows the Sekhokong gully sidewall exposing the sedimentary profile from which the SEK2014 and SEK2016 samples were retained. Stratigraphic logs presented against the age (kyr cal. BP) are presented for the two sequences. The SEK2014 stratigraphy is based on the carbon content and the grain size analysis in combination with a stratigraphic log against depth presented in Fitchett et al. (2016b). The discrete SEK2014 samples are marked out as red dots. The SEK2016 stratigraphy is based on visual core description.

Samples (SEK2016) were taken from the lower part of the gully, where over 4 meters of the deposit have been cut through and exposed (Figure 2 and 3). The outer layer of sediment was removed from the gully wall to get a fresh sampling surface. Core 1 (C1) and Core 3 (C3) were sampled by cutting sediment from an opened surface, using a knife (Figure 4). Samples were taken in triplicates dedicated to 1) XRF, 2) pollen and 3) microbial analysis with a resolution of approximately 2 to 3 cm. Core 2 (C2) was taken with a Russian corer from the gully base. The sampling depths were measured by tying a string across the gully as a reference for the deposit surface.

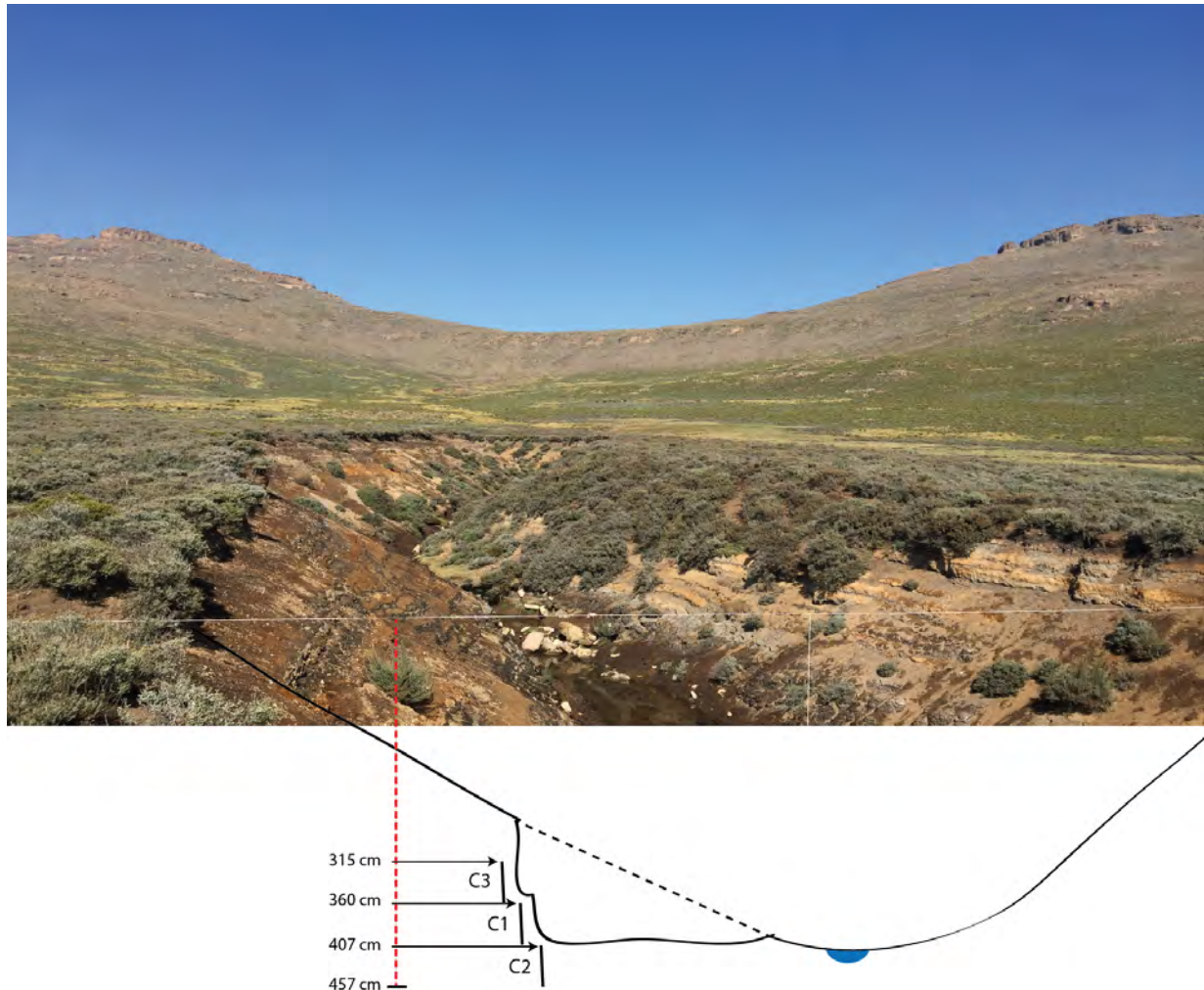


Figure 3 shows the study area, with the gully cutting through the deposit in Sekhokong Mountain range, Lesotho Highlands. The image is taken towards the south showing the north-facing slope of the Sekhokong range. The figure also schematically illustrates the sampling of the three cores making up the SEK2016 sequence.

Before analysis, the SEK2016 samples were sub-sampled at approximately 1 to 1.5 cm resolution and freeze-dried. The bulk density was calculated by multiplying the height and the surface area, which was estimated by drawing the outlines of the sample on a paper with known density. The bulk density was then estimated by dividing the dry weight by the volume. Samples were then milled (approximately 2 min at 30 strokes per minute) using a Lab Wizz Type 320 Micro Ball Mill.



Figure 4 shows the sediment samples from SEK2016 core 1 (bottom) and SEK2016 core 2 (top) reconstructed to a continuous sequence. The top of the core is at 0 cm (left).

4.1. Radio carbon dating and age model construction

Five samples were sent to the Ångström laboratory at Uppsala University and four samples were sent to Beta Analytic Inc. in Miami, FL USA, for age dating (Table 1). Due to a lack of macrofossils the ^{14}C dating in the previous study by Fitchett et al. (2016b) was based on bulk samples. In order to maintain consistency, the ^{14}C dating in this study was also based on bulk samples. If any macrofossils were existent, they were removed prior to the analysis. Samples were treated with 1% HCl for 8-10 hours to remove carbonates and then treated with 1% NaOH for 8-10 hours. The soluble portion precipitates when concentrated HCl is added. This soluble part was then washed and dried, used for analyses with an accelerator mass spectrometer (AMS). However one sample, SEKC15b, contained a larger amount of plant remains. Two age dates were therefore done for sample SEKC15b; one on the plant remains and one on the soluble part as previously described.

Table 1. The sample information and AMS radiocarbon dates from the Ångström laboratory (Ua-) and Beta Analytic Inc (Beta-). All samples are from the SEK2016 sequence. The calibration was done using the SHCal13 (Hogg et al. 2013) with 95% confidence intervals.

Lab ID	Sample No.	Radiocarbon age (¹⁴ C age BP)	Uncertainty	Calibrated age range (cal. BP)	Depth (cm)	Organic carbon (%)
Ua-54862	SEKC31a	11,632	57	13,299 – 13,548	315.625	23
Beta-466037	SEKC310b	12,110	40	13,770 – 14,063	338.5	20
Ua-54863	SEKC323	12,304	61	13,976 – 14,562	359.3	30
Beta-466034	SEKC15b	12,360	40	14,080 – 14,614	372.875	30
Beta-466735	SEKC15b	12,470	40	14,202 – 14,875	372.875	30
Ua-54859	SEKC111a	13,019	65	15,271 – 15,764	387.125	15
Ua-54860	SEKC27	13,500	68	15,955 – 16,449	416.75	12
Beta-466035	SEKC215	13,650	40	16,210 – 17,255	428.75	7
Ua-54861	SEKC226	14,033	72	16,650 – 17,255	445.25	6
Beta-466036	SEKC233	12,630	40	14,688 – 15,154	456	1,5

The age-depth model for SEK2016 was produced using Clam v.2.2 (Blaauw, 2010) in R statistical software. The ¹⁴C dates were calibrated using the southern hemisphere calibration curve SHCal13 by Hogg et al. (2013). For additional information of the age-depth model settings see Appendix A.

4.2. Carbon, nitrogen and stable carbon isotope analysis

All SEK2014 samples and approximately every second SEK2016 samples were analysed using a Finnigan Delta V advantage flow mass-spectrometer coupled to a CarloErba CN25000 elemental analyser (Department of Geological Sciences, Stockholm University) to quantify the concentrations of TOC, N and the stable isotopic value of ¹³C. Since carbonate was identified by LOI analysis, all samples were weighed in silver cups and acid treated with HCl (2M) in oven at 60 °C overnight prior analysis. The method has a standard deviation of <3% for TOC and N quantification and 0.15‰ for δ¹³C isotope values.

4.3. XRF analysis

All SEK2014 samples and approximately every second SEK2016 sample were analysed using a Bruker S8-Tiger WD-XRF (wavelength dispersive X-ray fluorescence) analyser equipped with a Rh-anticathode x-ray tube to obtain absolute elemental concentrations of the samples according to Rydberg (2014). Approximately 500 mg of freeze-dried and milled sample were put in Teflon cups sealed with a 2 µm Mylar film. The analyses were done by Johan Rydberg

in February 2017, at the Department of Ecology and Environmental Sciences at Umeå University. Every 10th sample were analysed in duplicate and a certified standard (CRM NCS DC-70314) was used. The precision was <10% for 15 elements (Al, Na, Mg, Si, K, Ti, P, Ca, Mn, V, Fe, Ni, Cu and Zn), between 10 to 30% for 5 elements (S, Sc, Co, Br, Sr) and between 30 to 80% for 4 elements (Cl, Cr, Ga, Ba). The accuracy was <10% for 17 elements (Al, Na, Mg, Si, K, Ti, P, Ca, Mn, V, Fe, Ni, Sr, Ga, Br, Ba and Zn), between 10 to 30% for 5 elements (S, Sc, Cr, Co and Cu) and 78% for Cl (see Appendix C for statistical data given for the specific elements).

4.4. FTIR-ATR analysis

All SEK2014 and SEK2016 were analysed by Infrared spectroscopy, using an Agilent Technologies Cary 630 FTIR equipped with an ATR device with a single-reflection diamond crystal at the Department of Edaphic and Chemical Agronomy at the University of Santiago de Compostela, Spain. The measurements were done within the wavelength spectral range of 4000 cm^{-1} to 400 cm^{-1} . The number of background scans were set to 64 and the number of sample scans were set to 150, all with a resolution of 4 cm^{-1} . The background was collected between every sample. The data was analysed in triplicate, with a correlation between the replicates >0.9.

4.5. XRD analysis

Nine selected samples (based on the FTIR-ATR and elemental data) were analysed with XRD, using a Philips type powder diffractometer fitted with Philips “PW1710” control unit, Vertical Philips “PW1820/00” goniometer and FR590 Enraf Nonius generator at the Department of Edaphic and Chemical Agronomy at the University of Santiago de Compostela, Spain. The instrument was equipped with a graphite diffracted beam monochromator and copper radiation source ($\lambda(K\alpha_1) = 1.5406\text{Å}$), operating at 40 kV and 30 mA. The XRD was scanned from 2° to $65^\circ 2\theta$ using a step size of 0.02° and counting time of 2 seconds per step.

4.6. Biogenic silica extraction and identification

Ten samples were selected to determine if the BSi, identified by FTIR-ATR and Si/Ti ratio, was controlled by diatoms. The silt-sized fraction (which is the size of siliceous microfossils, such as diatoms) was extracted and visually analysed under light microscope. The extraction was done on 1-2 g of untreated frozen samples. Carbonates were removed with HCl (10%) before H_2O_2 (17%) was added and left over night at room temperature. The samples and H_2O_2 (17%) were then gradually heated to 100°C in a waterbath until the OM dissolved and the liquid was clear. Milli-Q water was added and all particles were re-suspended. After 2 hours silt and sand sized particles had sedimented and the water and clay fraction were decanted. The decantation was repeated several times, until the water was clear (after 2 hours). To remove sand the sample was suspended and left for 5 seconds before decanting, where the particles left in the beaker were removed. The decanting step was then done once using weak NH_3 to remove remnants of clay. Thereafter decanting with Milli-Q water was performed until the water became clear after 2 hours. Using the remaining material, microscope slides were prepared and fixed with Naphrax heated to 200°C . The samples were visually analysed under an Olympus CH light microscope.

4.7. Statistical analysis

4.7.1. FTIR-ATR data

Principal component analysis (PCA) was performed on the transposed data matrix (i.e., samples as columns and spectral bands as rows) of the FTIR-ATR measurements using a varimax rotation. By performing PCA on the transposed matrix, the main constituents in the individual samples could be identified based on the variation in the spectroscopic signal, which is provided as a loading or an “estimated statistical weight”. The PCA scores can identify the constituents responsible for each principal component, where positive scores are higher than average absorbance and negative scores are lower than average absorbance. The main positive score peaks representing high absorbance within specific spectral bands can then be related to a chemical component. A combination and co-occurring of peaks is in most cases very crucial. Five principal components were extracted for the SEK2016 sequence and three for the SEK2014 sequence. The selection of numbers of components was based on a combination of the total variance, Kaiser threshold (eigenvalues > 1) and on the value of interpretation (the relevance for the components for the specific study).

4.7.2. Elemental geochemistry data

Since conventional XRF analysis and C/N analysis was not performed on all samples from the SEK2016 sequence, linear regression analyses were used to predict the missing values. The “STAT” package in R statistical software was used to fit linear models for the XRF, C and N data, (see Appendix B for the models used for each element). The results from the PCA of the FTIR-ATR data were used as predictors. The first and second components were combined to one predictor since they had a high negative correlation. After predicting the missing values in the SEK2016 elemental data, a PCA was applied using the varimax rotation where three principal components were extracted. A PCA was also performed on the elemental data from the SEK2014 sequence where one principal component was extracted. The extractions were based on a combination of the total variance, Kaiser threshold and the value of interpretation.

5. Results

The same set of analyses was applied to both SEK2014 and SEK2016 with the main difference being that SEK2016, which overlaps with the oldest portions of SEK2014, is continuous and has higher resolution. The sequences were divided into units based on major shifts within the geochemical data sets and the behaviour of the geochemical proxies. Three main categories of analyses were made: (i) organic chemistry (TOC, C/N and $\delta^{13}\text{C}$), (ii) FTIR-ATR analyses and (iii) conventional elemental data where PCA was applied to the latter two datasets. The FTIR-ATR data used a transposed matrix to acquire three principal components from SEK2014 (RC1₂₀₁₄-RC3₂₀₁₄) and five from SEK2016 (RC1₂₀₁₆-RC5₂₀₁₆) while the conventional XRF data extracted one principal component from the SEK2014 (PC1₂₀₁₄) and three from SEK2016 (PC1₂₀₁₆-PC3₂₀₁₆). These data are complimented by Si/Ti ratios, XRD analyses and diatom extractions, with the two latter made on selected SEK2016 samples.

5.1. SEK2014

The sediment of the SEK2014 sequence varies with depth, going from iron rich sandy silt layers with sections containing gravel, to organic rich brown layers and peat back to inorganic layers (Figure 2). The stratigraphy was constructed from the result of the sedimentary analyses obtained by Fitchett et al. (2016b). The SEK2014 sequence was subdivided into two units, Unit 1 and Unit 2, based on the major shifts and behaviour of the geochemical data. Unit 2 spans from 16,350 to 13,280 cal. BP, which corresponds approximately to the timeframe covered by the continuous SEK2016 sequence. Unit 1 spans from 13,280 cal. BP to present.

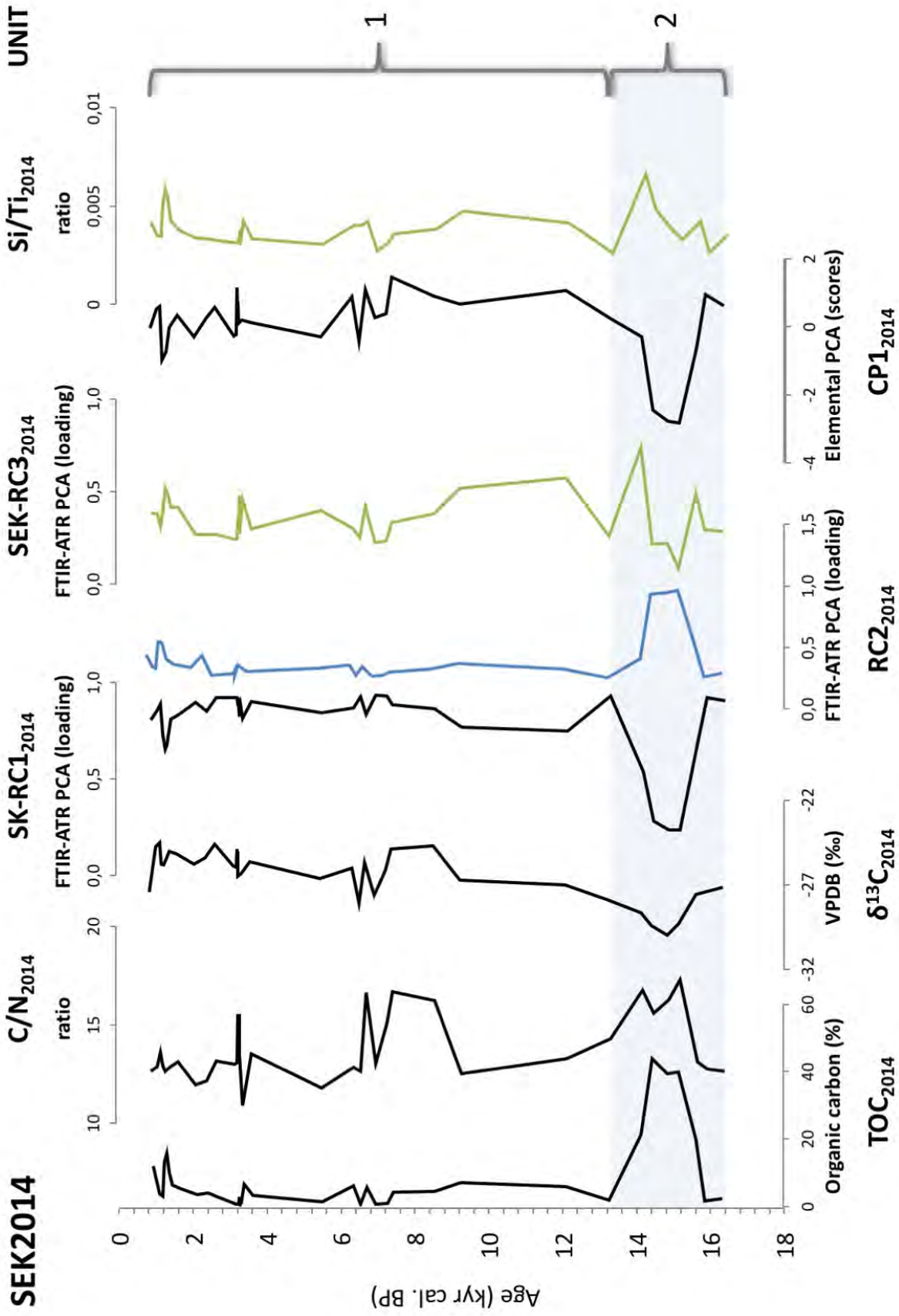


Figure 5 presents all the results from the SEK2014 sequence against depth; TOC (total organic carbon) content in %, the C/N ratio, $\delta^{13}\text{C}$ (stable carbon isotope values) in ‰, RC1₂₀₁₄, RC2₂₀₁₄ and RC3₂₀₁₄ (the principal components extracted from the FTIR-ATR PCA) loadings, CP1 (the principal component extracted from the elemental PCA) scores and Si/Ti ratio (from the XRF analysis). The identified units are marked out.

5.1.1. Organic chemistry: TOC, C/N ratios and $\delta^{13}\text{C}$

Figure 5 shows all the geochemical proxy data from SEK2014 against age. The major shifts seen in TOC_{2014} content occurs in Unit 2, with values increasing rapidly from 2% to 40%, within approximately 700 years (Figure 5). The TOC_{2014} level increases slightly during the following 700 years, reaching a maximum of 44% before it rapidly decreases back to 2% from 14,440 cal. BP to 13,280 cal. BP. The TOC_{2014} level fluctuates between values <1% and 7% for the entirety of Unit 1, except in the upper portion where it reaches a value of 16% in one sample. Generally, there are slightly higher values in the first half of Unit 1 compared to the second half. In Unit 1, four peaks can be identified at 6,720 cal. BP, 6,370 cal. BP, 3,400 cal. BP and 1,320 cal. BP, reaching TOC_{2014} values of 6%, 6%, 7% and 16%, respectively.

The C/N_{2014} ratios in the SEK2014 sequence shows increasing values in Unit 2, with values going from <13 to over 17 followed by a decrease to 14 (Figure 5). Unit 1 mainly shows C/N_{2014} values fluctuating between 12 and 14, with peaks at 8,560 to 7,430 cal. BP, 6,720 cal. BP and 3,280 cal. BP all reaching values around 16. There is also one noticeable C/N_{2014} ratio decrease (<11) at 3,400 cal. BP.

The $\delta^{13}\text{C}_{2014}$ values decrease in Unit 2, going from -27‰ at 15,630 cal. BP to -30‰ at 15,850 cal. BP and increase to -28‰ at 14,150 cal. BP (Figure 5). There is a general increasing trend throughout the entire Unit 1, with $\delta^{13}\text{C}_{2014}$ values going from -28‰ to <-25‰. There is one peak in the middle of Unit 1 that reaches <-25‰.

5.1.2. FTIR-ATR PCA

Figure 6 show the spectral signature for the three extracted principal components from the SEK2014 FTIR-ATR PCA, with scores plotted against the absorbance. Figure 6A presents the absorbance spectra for RC1_{2014} that shows the main peaks at 3550 cm^{-1} , 1000 cm^{-1} , 900 cm^{-1} , and 520 cm^{-1} . Figure 6B shows the absorbance spectra for RC2_{2014} with peaks at 3200 cm^{-1} , 2919 cm^{-1} , 2851 cm^{-1} , 1621 cm^{-1} , and 1034 cm^{-1} . Figure 6C shows the absorbance spectra for RC3_{2014} with the main peaks at 1100 cm^{-1} , 792 cm^{-1} , and 466 cm^{-1} .

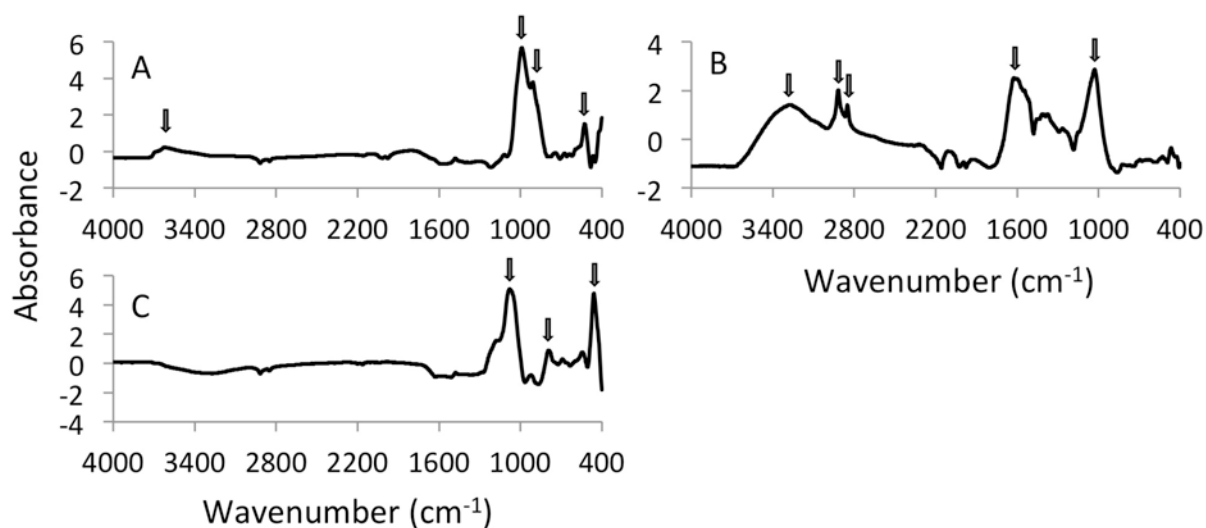


Figure 6 shows score plots for the three principle components extracted from the SEK2014 FTIR-ATR PCA. The scores (wavenumber, cm^{-1}) are plotted against the absorbance, giving the spectral signature for the various components. The main characteristic peaks are marked with arrows.

The three first components identified by PCA of the SEK2014 FTIR-ATR data explain 99% of the variance. Figure 5 show the loadings from the FTIR-ATR PCA against time. $RC1_{2014}$ values show a rapid decrease in Unit 2, from 0.9 at 15,870 cal. BP to 0.2 at 15,150 cal. BP where they are relatively stable for approximately 700 years before they increase back to 0.9 during 14,440 to 13,280 cal. BP. The $RC1_{2014}$ values decrease in the beginning of Unit 1, to values between 0.7 and 0.8. After 9,280 cal. BP, the values increase to 0.9, and stay relatively stable for the rest of Unit 1, with some decreasing fluctuations at 6,720 cal. BP (0.8), 3,410 cal. BP (0.8) and 1,320 cal. BP (0.6). $RC2_{2014}$ values rapidly increase in Unit 2 from <0.3 at 15,870 cal. BP to 1.0 at 15,150 cal. BP where they are stable for approximately 700 years before they rapidly decrease to 0.4 during 14,440 to 14,150 cal. BP and to <0.3 at 13,280 cal. BP. $RC2_{2014}$ values increase slightly in the beginning of Unit 1 and reach values close to 0.4. After 9,280 the $RC2_{2014}$ values decrease to <0.3 and remain relatively stable for the rest of the unit, with some fluctuations at 6,720 cal. BP (0.3), 3,410 cal. BP (0.4), 2,440 cal. BP (0.4) and 1,320 cal. BP (0.5). $RC2_{2014}$, shows a strong correlation with the absolute TOC values, $r = 0.96$ ($n = 37$ and p -values = $2.2e^{-16}$). $RC3_{2014}$ values have two major peaks in Unit 2, one at 15,630 cal. BP and one at 14,150 cal. BP, reaching values of 0.5 and 0.7, respectively. There is an increase of $RC3_{2014}$ in the lower half of Unit 1, with values around 0.5. In the upper part of Unit 1 there are three peaks at 6,720 cal. BP, 3,310 cal. BP and 1,320 cal. BP that reach 0.4, 0.5 and 0.5, respectively.

5.1.3. Elemental PCA

The first and only principal component extracted from the SEK2014 elemental PCA, CPI_{2014} , explains 47% of the variance. CPI_{2014} shows large positive loadings of Al, Ga, K, Si, Sc, Ti, Ni, Cr, Ba and Na, and large negative loadings of C, N, Br, Cl and S (Appendix C provides a table with the loadings for individual elements). Figure 5 shows CPI_{2014} scores against time. In Unit 2 the CPI_{2014} values decrease from 0.9 at 15,870 cal. BP to -0.3 at 15,150 cal. BP. CPI_{2014} values remain low until 14,440 cal. BP when they increase and reach 0.2 at 14,150 cal. BP. In Unit 1 the CPI_{2014} values fluctuate between 1.0 and -1.0 showing a slightly decreasing trend with time. There is one greater peak at 7,430 cal. BP reaching 1.5 and two distinct and narrow peaks at 3,310 cal. BP and 3,280 cal. BP reaching 0.7 and 1.2, respectively.

5.1.4. Si/Ti ratio

The Si/Ti_{2014} ratio based on conventional XRF data has two main peaks in Unit 2, at 15,630 and 14,150 cal. BP (Figure 5). The Si/Ti values in Unit 1 show a slight increase in the first half and then a decrease in the second half with three peaks at 6,720 cal. BP, 3,400 cal. BP and 1,320 cal. BP. The Si/Ti_{2014} and $RC3_{2014}$ show a strong correlation, $r = 0.72$ ($n = 37$ and p -values = $6.331e^{-07}$)

5.2. SEK2016

The sediment of the SEK2016 sequence varies throughout the core, going from iron rich sandy silt layers with sections containing gravel, to organic rich brown layers with distinct red lamination and pale layers (Figure 2, 8, 9 and 11). Based on the results of the analysed suite of geochemical variables four distinct units were identified. The different units represent the major shifts within the data profile, showing similar trends within the units themselves. Age dating of SEK2016 reveals that the sediment sequence spans from 17,335 to 13,440 cal. BP (Figure 7), covering parts of the last glacial-interglacial transition. Using the age model, Unit D spans from 17,335 to 16,115 cal. BP, Unit C from 16,115 to 15,315 cal. BP, Unit B from 15,315 to 14,175 cal. BP and Unit A from 14,175 to 13,440 cal. BP.

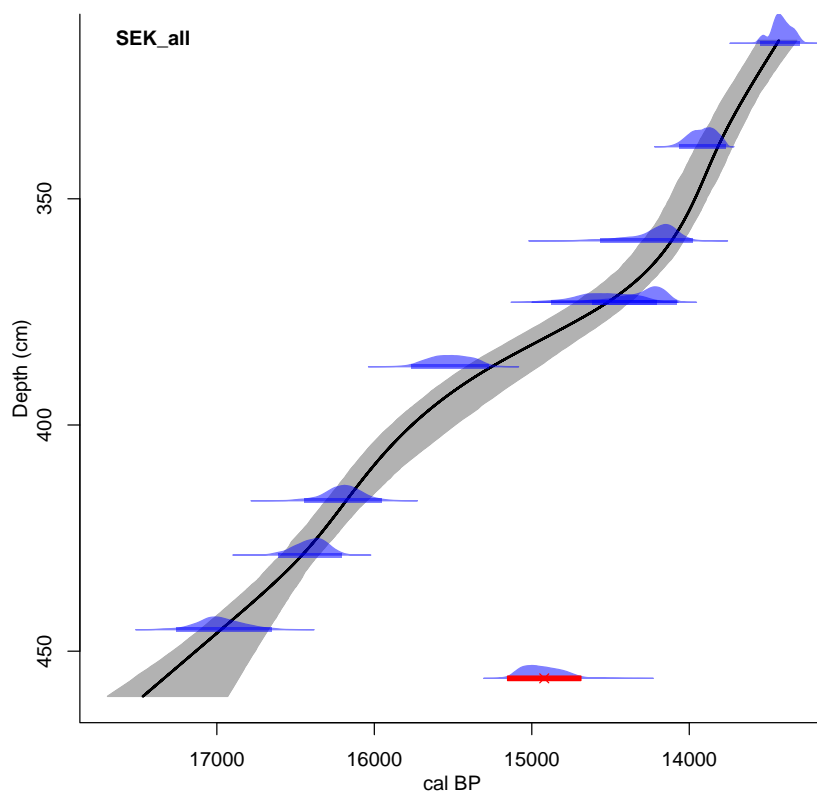


Figure 7. Age-depth model for SEK2016, produced using Clam v.2.2 (Blaauw, 2010) in R statistical software. The red mark indicates one outlier.

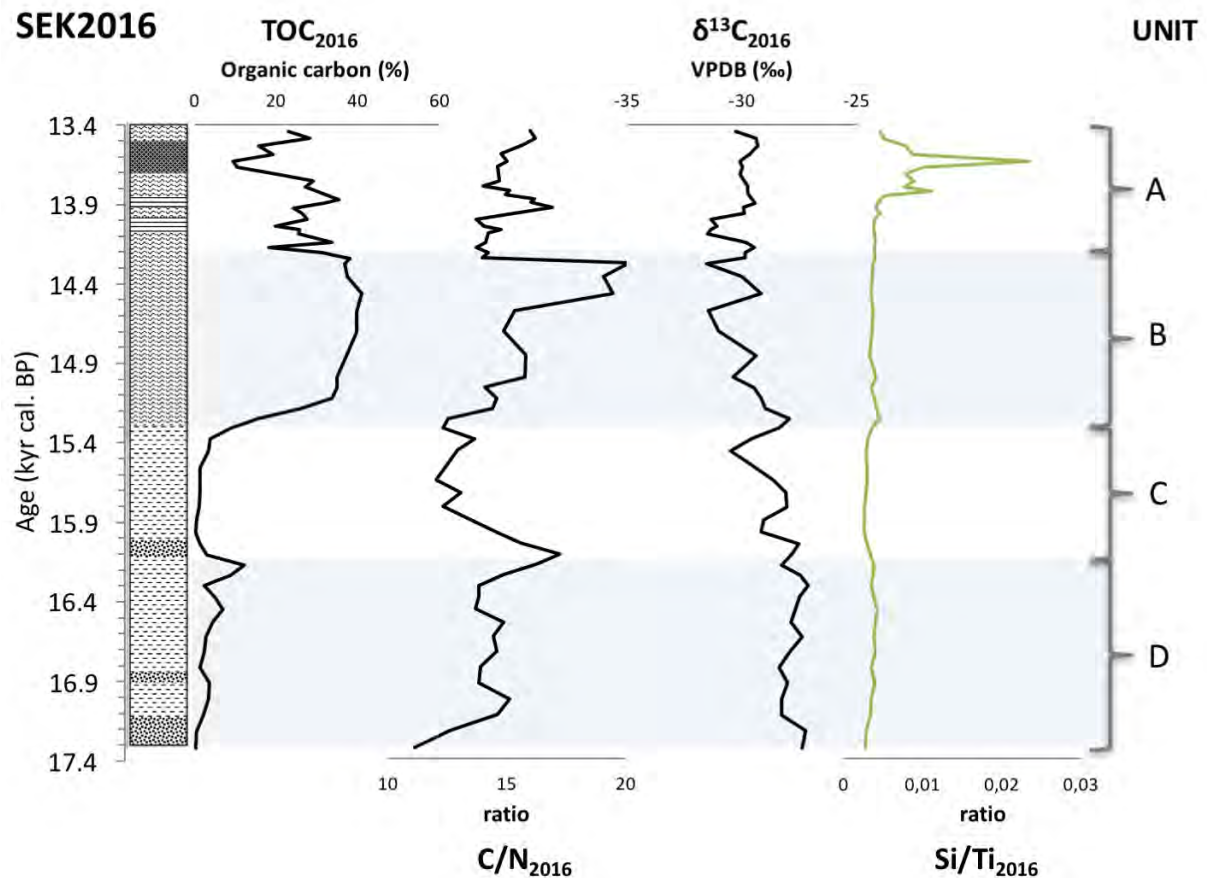


Figure 8. The organic geochemistry data for the continuous and high-resolution SEK2016 sequence against age (kyr cal. BP); TOC (total organic carbon) content in %, the C/N ratio, $\delta^{13}\text{C}$ (stable carbon isotope values) in ‰. The Si/Ti ratio is based on the XRF data. The identified units are marked out.

5.2.1. Organic chemistry: TOC, C/N ratios and $\delta^{13}\text{C}$

TOC₂₀₁₆ varies significantly throughout the sequence. Unit D has relatively low TOC₂₀₁₆ values around 3%. Concentrations increase from 0.4% in the bottommost section with several fluctuations, reaching TOC₂₀₁₆ values of over 12% at 16,180 cal. BP. TOC₂₀₁₆ decreases in the beginning Unit C to values below 1.4%, which is the lowest values seen within the entire sequence. At the end of Unit C and the beginning of Unit B there is a major shift in TOC₂₀₁₆ values, going from 3% at 15,385 cal. BP to 35% at 15,135 cal. BP. The TOC₂₀₁₆ values continues to increase, reaching the sequence maximum of approximately 40% at 14,575 cal. BP. However, TOC₂₀₁₆ values stay relatively stable from 15,135 to 14,240 cal. BP, when they decrease to 18% at 14,175 cal. BP. Unit A shows multiple fluctuations with TOC₂₀₁₆ values between 9% and 35%.

In Unit D, the C/N_{2016} ratio varies between 11 and 20 throughout the entire unit. Unit D begins with low C/N_{2016} values around 11 that increase to 15 at 17,125 cal. BP. The values fluctuate slightly between 14 and 15 until the end of Unit D where the C/N_{2016} ratio reaches 16 at 16,180 cal. BP. This excursion peaks in the beginning of Unit C, reaching C/N_{2016} values >17 . The C/N_{2016} values decrease and stay relatively low between 12 and 14, for the majority of Unit C, which is the section that shows the lowest values (with the exception of a short period early in Unit D). Unit B shows an increasing trend in C/N_{2016} values, going from approximately 12 at 15,315 cal. BP in the beginning of the unit to 20 at 14,465 to 14,276 cal. BP before it makes a rapid drop back to 14 at 14,240 at the end of Unit B. The most significant increase in C/N_{2016} values can be seen in the later part of Unit B, from 14,575 to 14,465 cal. BP, where it goes from 15 to 19. Unit A has C/N_{2016} values mainly varying between 14 and 16, with a small peak reaching 16 at 13,925 cal. BP and a slight increase in the end of the unit, also reaching values of 16.

The stable $\delta^{13}C_{2016}$ values show a slightly increasing trend with time, going from -27.4‰ to -30.3‰, reaching values as low as -31.5‰ in Unit B (Figure 8).

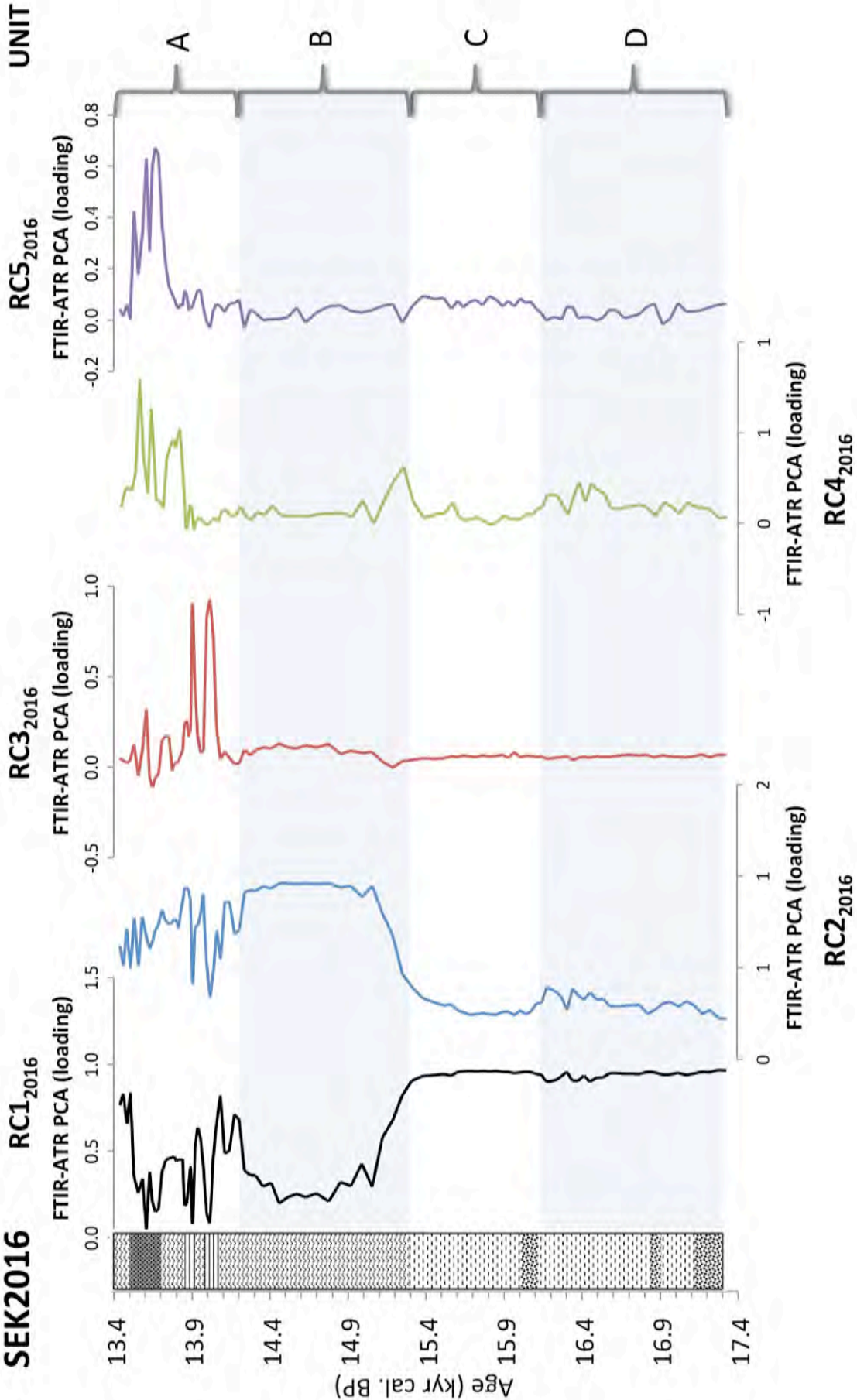


Figure 9 shows the loadings for the five extracted components from the SEK2016 FTIR-ATR PCA against age (kyr cal. BP). The identified units are marked out.

5.2.2. FTIR-ATR PCA

Figure 10 shows the spectral signature for the five extracted principal components RC1₂₀₁₆-RC5₂₀₁₆ from the SEK2016 FTIR-ATR PCA, where the scores are plotted against absorbance. Figure 10A, shows the main absorbance spectra for RC1₂₀₁₆ with the main peaks at 3550 cm⁻¹, 1000 cm⁻¹, 900 cm⁻¹ and 520 cm⁻¹. The main absorbance peaks for RC2₂₀₁₆ are shown in Figure 10B, at 3200 cm⁻¹, 2919 cm⁻¹, 2851 cm⁻¹, 1621 cm⁻¹, and 1034 cm⁻¹. RC2₂₀₁₆, shows a strong correlation with the absolute TOC values, $r = 0.95$ ($n = 59$ and $p\text{-value} = 2.2e^{-16}$). Figure 10C, presents the spectral signature for RC3₂₀₁₆ with the key absorbance peaks at 1400 cm⁻¹, 859 cm⁻¹ and 738 cm⁻¹. Figure 10D presents RC4₂₀₁₆ that shows the main absorbance peaks at 1100 cm⁻¹, 980 cm⁻¹, 792 cm⁻¹, and 466 cm⁻¹. The absorbance spectra for RC5₂₀₁₆ is presented in Figure 10E, showing the main absorbance peaks at 1621 cm⁻¹, 1398 cm⁻¹ and 861 cm⁻¹. These five components identified by the PCA applied to the SEK2016 FTIR-ATR data explain 97% of the variance.

Figure 9 shows the loadings from the SEK2016 FTIR-ATR PCA against age. RC1₂₀₁₆ values are high and stable around 0.9 in Unit D and Unit C. There is a major shift at the beginning of Unit B where RC1₂₀₁₆ values decrease from 0.9 at 15,315 cal. BP to 0.3 at 15,060 cal. BP. RC1₂₀₁₆ values remain relatively low, around 0.3 for the most of Unit B, until they increase to 0.7 at 14,210 cal. BP. In Unit A, the RC1₂₀₁₆ values fluctuates from approximately 0.8 to 0.1, with the highest values in the beginning and at the end of the unit. RC2₂₀₁₆ values show a slightly fluctuating increase from 0.2 to 0.4 in unit D. In Unit C there is a decrease in RC2₂₀₁₆ values, reaching the lowest values seen within the sequence. The rapid shift seen in RC1₂₀₁₆ values during 15,315 to 15,060 cal. BP at the beginning of Unit B, can also be seen in the RC2₂₀₁₆ values that increase from 0.4 to 0.9 over approximately 300 years. RC2₂₀₁₆ values stay high and stable until 14,240 cal. BP where they decrease and reach 0.7 at 14,210 cal. BP. RC2₂₀₁₆ values are between 0.9 and 0.4 in Unit A. RC3₂₀₁₆ values are stable around 0 during Unit D and Unit C. There is a slight increase of in RC3₂₀₁₆ values in Unit B, reaching values around 0.1. The RC3₂₀₁₆ data shows two major peaks at the beginning of Unit A that reach 0.9 at 14,020 cal. BP and at 13,910 cal. BP. In the second half of Unit A RC3₂₀₁₆ fluctuates between -0.1 and 0.3.

RC4₂₀₁₆ values show an increasing trend in Unit D, with values going from 0 to 0.2. In Unit C there is a decrease in the RC4₂₀₁₆ values, reaching 0.0 which is the lowest values seen within the sequence (except a few samples in Unit D). In the beginning of Unit B, there is a moderate excursion in RC4₂₀₁₆, reaching values around 0.3 at 15,255 cal. BP. The rest of Unit B shows RC4₂₀₁₆ values <0.1. RC4₂₀₁₆ shows three major peaks in Unit A, reaching 0.5 at 13,765 cal. BP, 0.6 at 13,635 cal. BP and 0.8 at 13,560 cal. BP. RC5₂₀₁₆ values are relatively low in Unit D, Unit C and Unit B, with slightly higher values seen during Unit C. There are three peaks seen in RC5₂₀₁₆ in Unit A, two with values >0.6 and one with value 0.4, at 13,690 cal. BP, 13,610 cal. BP and 13,535 cal. BP, respectively.

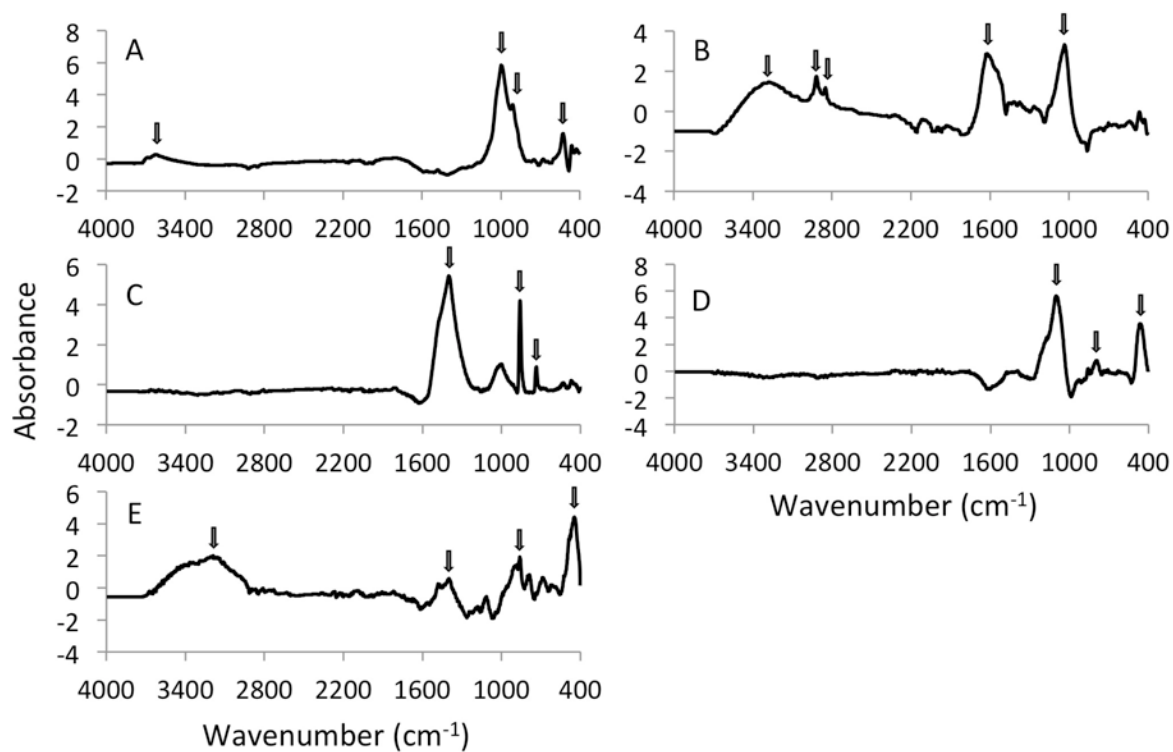


Figure 10 shows score plots for the five principle components extracted from the SEK2016 FTIR-ATR PCA; A) shows the first component (RC1₂₀₁₆), B) the second component (RC2₂₀₁₆), C) the third component (RC3₂₀₁₆), D) the fourth component (RC4₂₀₁₆) and E) the fifth component (RC5₂₀₁₆). The scores (wavenumber, cm⁻¹) are plotted against the absorbance, giving the spectral signature for the various components. The main characteristic peaks are marked with arrows.

5.2.3. Elemental PCA

The first three principal components, CP1₂₀₁₆-CP3₂₀₁₆ extracted from the SEK2016 elemental PCA explain 92% of the variance. The first component CP1₂₀₁₆ shows large positive loadings of Na, Sr, Ba, Mg, Ti, Ca, Cr, Ga, K, Sc, Si, Al, Ni, Co, and large negative loadings of Cl, Br, C, N and S (Appendix C provides a table with the loadings for individual elements). The second component CP2₂₀₁₆ shows large negative loadings of Mn and Fe. The third component CP3₂₀₁₆ shows positive loading of Ni and negative loading of Fe.

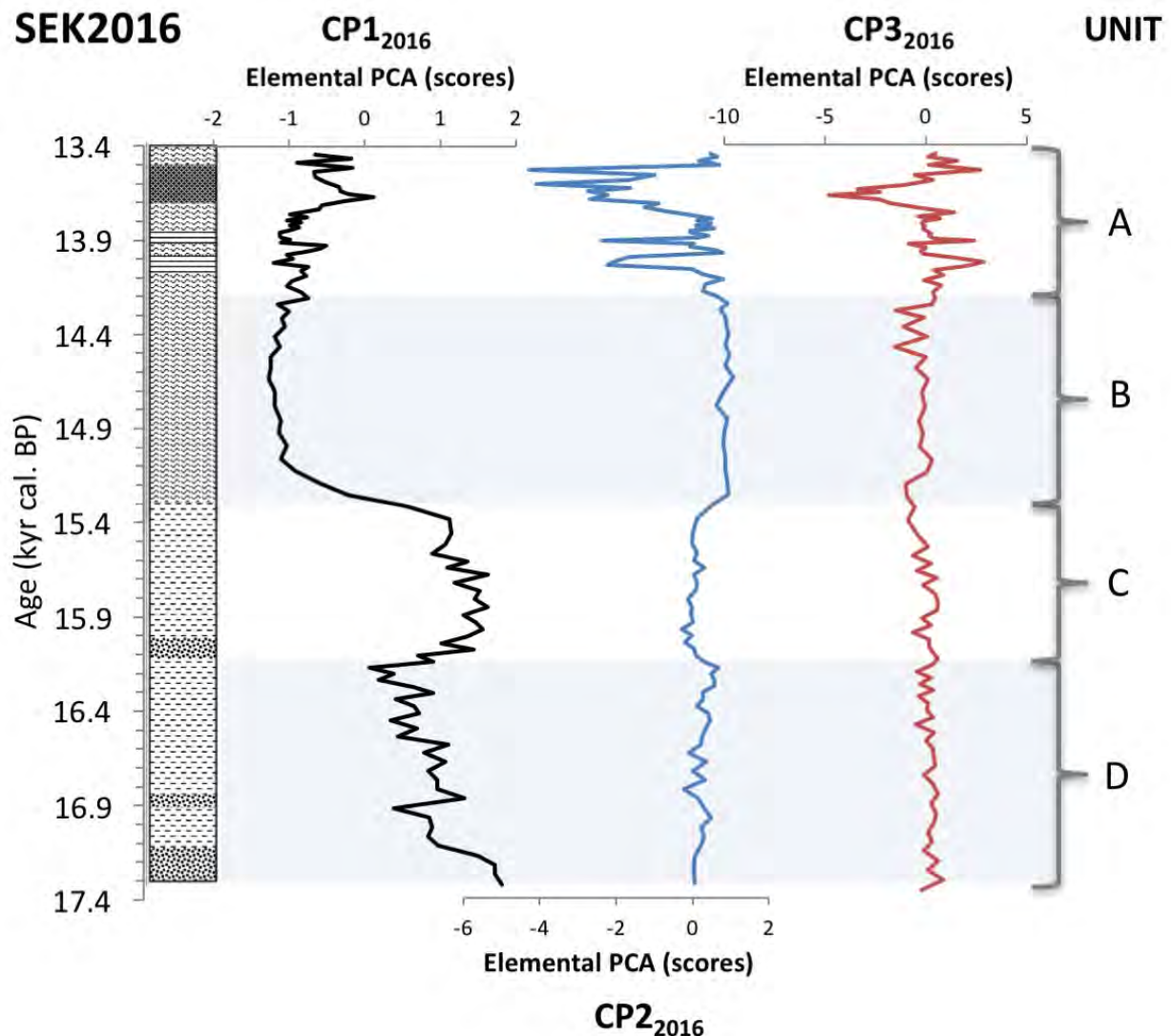


Figure 11 shows the scores from the elemental PCA of the SEK2016 sequence against age (kyr cal. BP). The identified units are marked out.

Figure 11 shows the SEK2016 elemental PCA scores against age. In Unit D, CP1₂₀₁₆ values fluctuate between 1.8 and 0.3 showing a decreasing trend with time until they rapidly increase to 0 at 16,235 cal. BP at the end of the unit. Unit C has relatively high and constant CP1₂₀₁₆ values >1.0 through most of the unit, until they rapidly decrease from 1.1 at 15,385 cal. BP to -1.0 at 15,125 cal. BP during the transition from Unit C to Unit B. CP1₂₀₁₆ values stay around

-1.0 for most of Unit B, with a slight increase after 14,240 cal. BP. In Unit A, the $CP1_{2016}$ values show a general increasing trend going from <-1.0 to approximately -0.2 . There are however two peaks reaching values of -0.5 and 0.1 at 13,925 cal. BP and 13,670 cal. BP, respectively. $CP2_{2016}$ shows unchanged values around 0 in Unit D with a decrease to -0.2 seen in Unit C. In Unit B the $CP2_{2016}$ increases back to values around 0. The major change in $CP2_{2016}$ can be seen in Unit A, with multiple negative peaks reaching values of -2.2 between 14,040 to 14,000 cal. BP, -2.4 at 13,910 cal. BP, -2.7 at 13,680 to 13,650 cal. BP, -4.0 at 13,610 cal. BP and -4.3 at 13,535 cal. BP. $CP3_{2016}$ values fluctuate between -0.3 and 0.8 through Unit D. In Unit C there is a slightly decreasing trend in the $PC3_{2016}$ values, going from 0.6 to -1.0 . $PC3_{2016}$ values increase at the beginning of Unit B and stay relatively stable around -0.1 until they decrease to -1.0 at the end of the unit. The major changes in $PC3_{2016}$ can be seen in Unit A, with three major peaks reaching 2.8 at 14,020 cal. BP, 2.4 at 13,910 cal. BP and 2.7 at 13,535 cal. BP. There is one negative peak between 13,780 to 13,585 cal. BP, reaching $PC3_{2016}$ values of -4.8 at 13,668 cal. BP

5.2.4. Si/Ti ratios

Si/Ti_{2016} ratio show relatively low values in Units D, C and B, with a decrease in Unit C reaching the lowest values seen within the profile (Figure 8). These low values last for the entire Unit C. There is a Si/Ti_{2016} ratio peak at 15,190 cal. BP in the beginning of Unit B. The largest variation occurs in Unit A, with a great increase after 13,845 cal. BP. This increase shows peaks at 13,820 cal. BP and 13,635 cal. BP. The Si/Ti_{2016} and $RC4_{2016}$ show a strong correlation, $r = 0.79$ ($n = 59$ and $p\text{-value} = 9.92e^{-14}$)

5.2.5. XRD

The results from the XRD analysis are presented in Figure 12A-C (Appendix D shows the remaining diffractograms). Figure 12A show data diffractograms for samples from 13,910 cal. BP (SEK2016-C14A) and 14,020 cal. BP (SEK2016-C319), both selected for analysis because of their relative increase in $RC3_{2016}$ (Figure 9). They show a pattern that corresponds to the siderite reference (Renard et al., 2017). Analyses made on SEK2016 samples dating to 13,790 cal. BP (SEK2016-C310A) and 15,255 cal. BP (SEK2016-C111A) are shown in Figure 12B. These samples were selected because they showed a relative increase in Si/Ti_{2016} and $RC4_{2016}$ (Figures 8 and 9). These two samples displayed a broad peak around $20\text{-}25^\circ$ in the XRD diffractogram. Figure 12C shows samples dating to 13,535 cal. BP (SEK2016-C33A) and 13,668 cal. BP (SEK2016-C36A), which were selected because they showed a relative increase in $RC5_{2016}$ (Figure 9). They show a pattern that corresponds to the goethite reference (Levien et al., 1980).

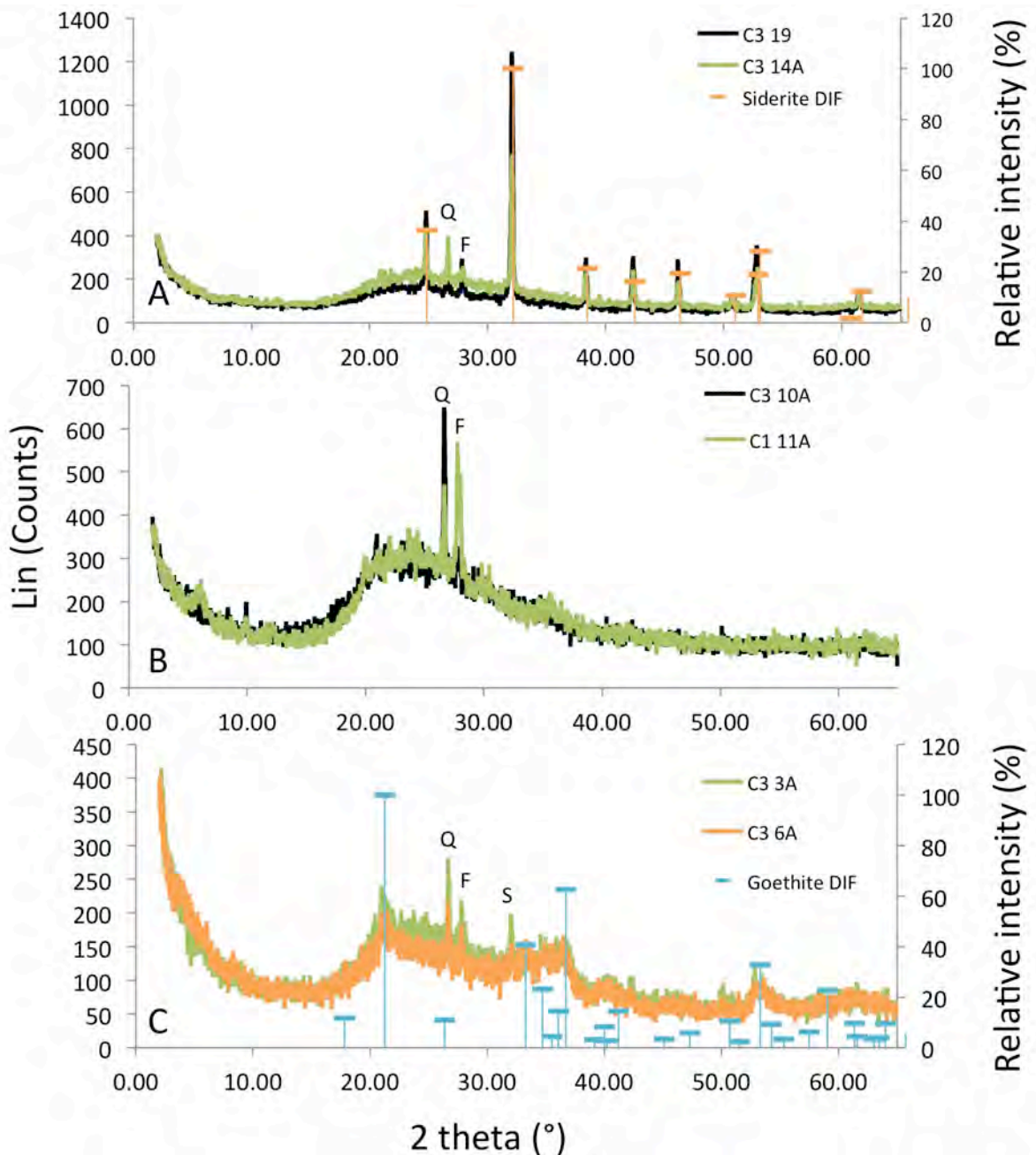


Figure 12. Diffractograms for the XRD analysis; A) the samples selected based on peaks in the RC₃₂₀₁₆ (SEK319 and SEKC14A) shown together with a siderite reference sample (Renard et al., 2017) B) shows the samples selected based on peaks in the RC₄₂₀₁₆ and Si/Ti₂₀₁₆ (SEKC310A and SEKC111A) and C) the samples selected based on peaks in the RC₅₂₀₁₆ (SEK33A and SEKC36A) are shown together with a goethite reference sample (Levien et al., 1980). Q = quartz, F = feldspar and S = siderite are indicating other significant peaks identified in the diffractograms.

5.2.6. Biogenic silica

Figure 13 shows four of the samples where the silt fraction, which include the BSi microfossils, were extracted and analysed under light microscope. These samples were selected due to their relative increase in $\text{Si}/\text{Ti}_{2016}$ and $\text{RC}_{4_{2016}}$ (Figure 8 and 9). Figure 13A and 13B, show samples from 13,650 cal. BP (SEK2016-C35) and 13,800 cal. BP (SEK2016-C310), respectively, which have very low relative content of diatoms and a high relative content of long elongated phytoliths. The phytoliths were identified based on morphological descriptions by Twiss et al. (1969). Figure 13C and 13D, 15,150 cal. BP (SEK2016-C110) and 16,450 cal. BP (SEK2016-C215), respectively, show that diatoms control the BSi content.

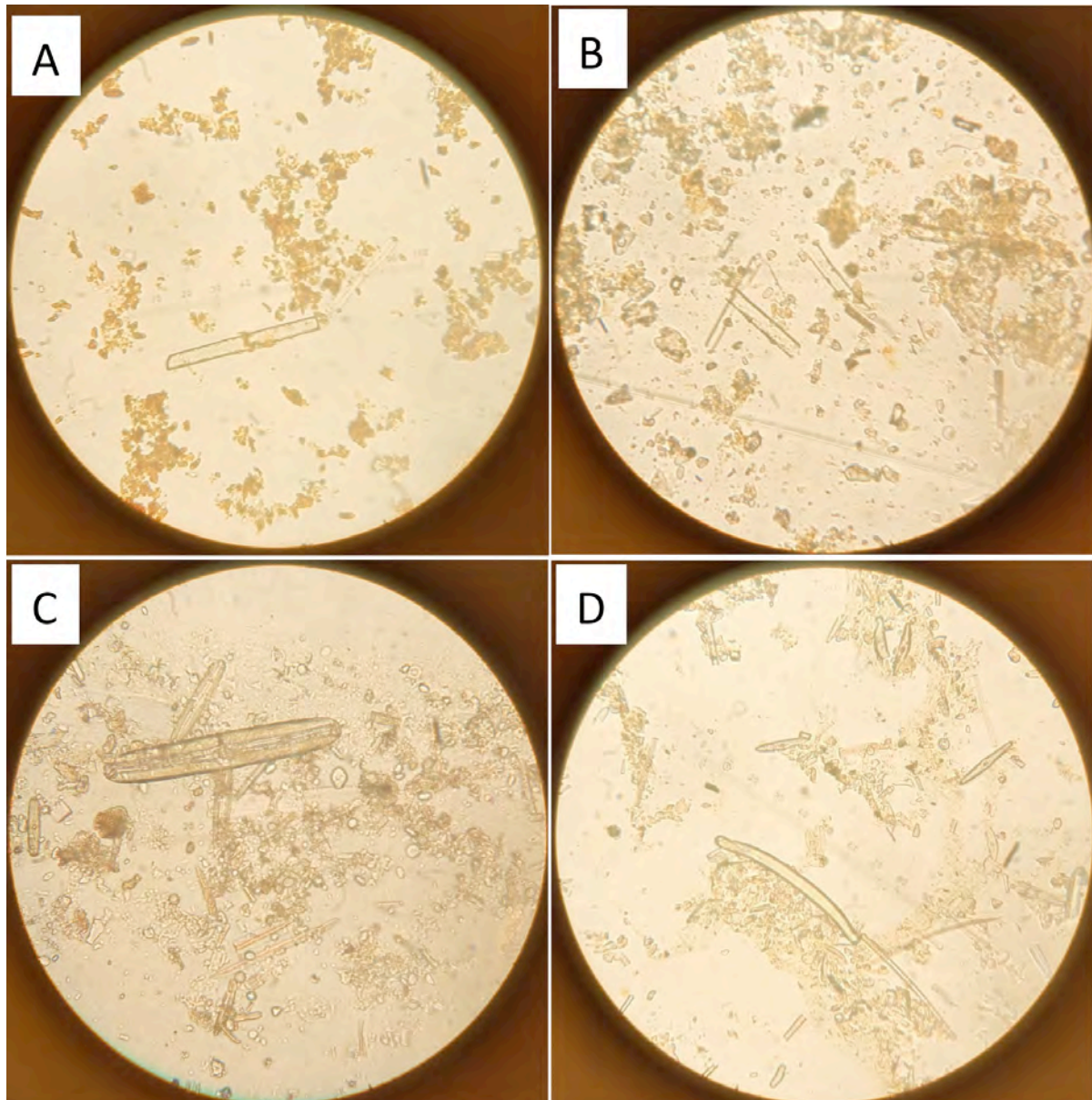


Figure 13 shows microscopic images with a 40× magnification using an Olympus CH light microscope. The selected images represent the general content of the samples. Image A and B present SEK2016-C35 and SEK2016-C310, respectively. Both samples have low diatom content and high abundance of long elongated phytoliths. Image C and D present SEK2016-C110 and SEK2016-C215, respectively and have a high diatom content.

6. Discussion

The Sekhokong wetland deposit is difficult to classify since it appears to have gone through quite dramatic variations over time with periods of higher standing water table, wetland and dry conditions (Marker, 1994). The following discussion starts by interpreting the geochemical signals identified by the organic chemistry, the FTIR-ATR PCA, the elemental PCA, and Si/Ti ratios from both the SEK2014 and the SEK2016 sequences. These proxies are then linked to the processes and environmental conditions responsible for the geochemical signals. This study is then put into a larger context by comparing the observed variations with other environmental reconstructions in the region spanning the same period of time.

6.1 Extraction of significant factors

The PCA reduces the number of variables by identifying and combining those variables that behave in a similar way and therefore, likely controlled by the same processes (Pérez-Rodríguez et al., 2016). There are different ways to proceed when determining the number of components to retain from the PCA analysis and multiple factors need to be considered. One option is to include components with an eigenvalue >1 , also called the Kaiser rule. A second is to make a scree test, by identifying a breaking point from a plot of the eigenvalues. The selection of components can also be done by deciding a minimum of variance for each component or for the total accumulated variance. The selected components should also fulfil the “interpretation criterion”, which is sometimes considered to be the most important way to determine the number of components. Different criteria were therefore used to determine the number of components for the different analyses completed.

For the PCA on the SEK2014 FTIR-ATR data the proportion of variance ($>5\%$ for each component), the scree test and the interpretability criteria agreed to the three first components being significant. For the PCA on the elemental data the three first rules, which are the objective rules, could not be used to determine the number of components in a way where it agreed with the interpretability criteria. For the PCA of the SEK2014 elemental data the Kaiser rule identified the first four components to be significant and the proportion of variance ($>5\%$ for each component) identified the first three components to be significant. However, component two, three and four did not fulfil the interpretability criteria and were not likely to contribute with any important geochemical information for the study and was therefore excluded from the result.

For the PCA of the SEK2016 FTIR-ATR data the Kaiser rule, the scree test and the interpretability criteria all agreed that the five first components were significant. For the PCA on the SEK2016 elemental data the Kaiser rule and the proportion of variance ($>5\%$ for each component) identified the first and the second component to be significant. However, the third component contributes with important geochemical information for the study and was therefore included in the result.

6.2. Interpreting the proxies

The following section will describe the interpretation of the proxies. Table 2 presents the components extracted from the PCA (both on the FTIR-ATR and elemental data set) and what they are associated with.

Table 2. Extracted components from all principal component analyses and their interpretation.

PCA	SEK2014	SEK2016	Association/description
FTIR-ATR	RC1	RC1	Clay minerals
	RC2	RC2	Organic compounds
	RC3	RC3	Siderite
		RC4	Biogenic silica
		RC5	Goethite
Elemental data	CP1	CP1	Inorganic matter (+) relative to organic matter (-)
		CP2	Iron-rich minerals, siderite and goethite (-)
		CP3	Distinguish between siderite (+) and goethite (-)

Table 3. Principal components extracted from the FTIR-ATR PCA and their main characterising peaks, the associated molecular bond and vibration as well as what component these absorption bands can be associated with.

PCA SEK2014	PCA SEK2016	Wavenumber (cm ⁻¹)	Peak assignment	Associated component	Reference
RC1 RC2	RC1 RC2 RC5	3700-3000	Stretching and bending vibrations O-H		(Müller et al., 2014) (Meyer-Jacob et al., 2014) (Cocozza et al., 2003)
RC1	RC1	1200-400	Stretching and bending vibration of SiO and Si-O-M (M=Al, Mg, etc.)	Clay minerals	(Müller et al., 2014)
RC2	RC2	2919 and 2851	Asymmetric stretching of C-H	Aliphatic	(Cocozza et al., 2003)
RC2	RC2	1621	C-O vibration C=O and COO ⁻ groups	Humic compounds Aromatics	(Kalbitz et al., 2000) (Cocozza et al., 2003)
	RC3	1400, 859 and 738	Asymmetric vibration, out-of-plane bending vibration and in-plane bending vibration of CO ₃ ²⁻	Carbonate	(Müller et al., 2014)
	RC5	1398	Fe-OH vibration	Iron hydroxide	(Rout et al., 2011)
RC3	RC4	1100	Asymmetric stretching vibration of SiO ₄	Biogenic silica	(Meyer-Jacob et al., 2014)
RC2	RC2	1034	C-O stretching	Polysaccharides	(Cocozza et al., 2003)
	RC5	861	Bending vibration of the hydroxyl groups of iron-oxide	Iron hydroxide	(Rout et al., 2011)
RC3	RC4	792	Symmetric stretching vibration of Si-O-Si	Biogenic silica	(Meyer-Jacob et al., 2014)
RC3	RC4	466	Bending vibration of SiO ₄	Biogenic silica	(Meyer-Jacob et al., 2014)

Table 3 presents all the main peaks identified in the score plots from the FRIT-ATR PCA (both sequences), as well as what molecular bond and the component/components associated with the specific wavenumbers. The first principal component identified in the FTIR-ATR PCA from both sequences, RC1₂₀₁₄ and RC1₂₀₁₆, is interpreted as IM, with a spectral signature typical for clay minerals (Müller et al., 2014) (Figure 6 and Table 3). RC2₂₀₁₄ and RC2₂₀₁₆ are interpreted to represent OM since they have spectral signatures with peaks recognising OH groups, aliphatic (fats, waxes and lipids), humic compounds, aromatics and polysaccharides (Cocozza et al., 2003; Kalbitz et al., 2000) (Figure 6 and Table 3). The RC3₂₀₁₆ signal is interpreted to be siderite (iron-carbonate; FeCO₃), as it has a spectral signature typical for carbonate (Müller et al., 2014) (Figure 6 and Table 3). The elemental data showed low concentrations of Ca and Mg but relatively high concentrations of Fe for the samples showing high RC3₂₀₁₆ loading, indicating that it is more likely that siderite, rather than calcium carbonate, is responsible for the spectroscopy signal. The presence of siderite in these samples was independently confirmed by XRD analysis (Figure 12A). Siderite formation is restricted to reducing conditions and high CO₂ partial pressure (Doner and Grossl, 2002), such as anoxic environments with high microbial oxidation of OM (Meyer-Jacob et al., 2014). The formation of siderite is often one of the first reactions to occur in the sediment, which makes the presence of siderite minerals a good proxy for reducing conditions in paleoenvironmental studies (Mozley and Wersin, 1992).

RC3₂₀₁₄ and RC4₂₀₁₆ are interpreted to signal the presence of BSi with the main characterising peaks previously used to identify diatoms in Meyer-Jacob et al. (2003) (Figure 6 and Table 3). The presence of BSi was independently confirmed by XRD analyses (Figure 12B), showing a diffraction pattern typical for opal-A, which is BSi formed by plants as phytoliths or skeletons formed by diatoms, radiolarian and sponges (Monger and Kelly, 2002). The elevated levels of BSi are also aligned with the elemental data and increased Si/Ti₂₀₁₄ and Si/Ti₂₀₁₆ (Figure 8). The variation in BSi abundance over time, may be a result of changes in productivity (Boyle, 2001; Takano et al., 2012). BSi is often used as a proxy for diatom abundance and generally an increase of diatoms would suggest higher productivity, indicating conditions with a relative increase in humidity (Finné et al., 2010). Since diatoms only stand for a part of the phytoplankton community, these variations may reflect changes within the community itself and not just the net productivity (Boyle, 2001; Takano et al., 2012). The possible input of phytoliths and other forms of BSi also needs to be taken into account. When comparing the samples responsible for the three main BSi peaks identified in SEK2016 (by Si/Ti₂₀₁₄ Figure 8 and RC4₂₀₁₆ Figure 9), it was clear that the main contribution of BSi in the samples varied, from being controlled by diatoms (Figure 13C and 13D) to being controlled by phytoliths (Figure 13A and 13B). Note however that the diatom relative to phytoliths abundance was estimated and no cell counting was done. However, this data gives a good indication of what controls BSi within the sequence.

RC5₂₀₁₆ represents variations in goethite (α -FeOOH, the most common Fe oxide in natural environments; Bigham et al., 2002) based on the absorption represented by vibration of OH groups, Fe-OH and hydroxyl groups of iron oxides (Rout et al., 2011) (Figure 6 and Table 3). The presence of goethite was independently confirmed by XRD analysis (Figure 12C).

Changes in goethite occur in parallel to CP2₂₀₁₆ and CP3₂₀₁₆ (discussed below). It can be difficult to use goethite as a proxy to reconstruct processes and paleoenvironmental conditions, since it is one of the most common iron-oxyhydroxides in natural environments (Bigham et al., 2002). There are multiple formation pathways, implicating different processes that require different conditions. However, the typical formation setting is under cool and wet conditions, usually at high altitudes like the Sekhokong Mountain Range (Bigham et al., 2002). Lowering of the pH and increased oxygen levels would favour precipitation of goethite over siderite (Dill and Techmer, 2009). Goethite is also associated with alteration of siderite (Akande and Mücke, 1993; Renard et al., 2017), thus it may be a result of post-diagenetic processes (Akande and Mücke, 1993; Middleton and Nelson, 1996).

The first principal components extracted from the elemental data, CP1₂₀₁₄ and CP1₂₀₁₆, distinguish between IM and OM, with high positive loadings associated with elements commonly found locked in silicate minerals (Berner and Berner, 1996) and high negative loadings associated with elements in organic molecules, respectively (Berner and Berner, 1996; Davies et al., 2015). CP2₂₀₁₆ shows highly negative loadings of Fe and Mg, which is interpreted to represent Fe (Mn is less abundant) incorporated minerals, such as siderite and goethite. Both Fe and Mn are redox sensitive elements that mobilise under anoxic conditions (Boyle, 2001). The negative CP2₂₀₁₆ peaks co-occur with RC3₂₀₁₆ and RC5₂₀₁₆ providing two independent datasets that identify these minerals. The third component, CP3₂₀₁₆, distinguishes between siderite and goethite based on chemical differences, due to nickel substituting for iron during siderite precipitation (Montes-Hernandez and Pironon, 2009).

6.3. Paleohydroclimatic interpretation

The following section will give a paleohydrological interpretation of the SEK2014 and the SEK2016 sequence, based on the proxy data. No separate interpretation will be presented from SEK2014 Unit 2 since SEK2016 covers the same section of the profile. However, the major trends seen in the SEK2016 data are also observed in the SEK2014 proxy data, such as the pronounced increase in OM (seen after 15,870 cal. BP in SEK2014) and BSi peaks (seen at 15,630 cal. BP and 14,150 cal. BP in SEK2014). The differences in resolution need to be considered when comparing the data sets.

6.3.1. SEK2016 Unit D: 17,335 to 16,115 cal. BP

In the beginning of Unit D there is relatively low OM (TOC_{2016} , RC_{2016} and decreasing CPI_{2016}) content and high IM (RC_{12016} and CPI_{2016}) content suggesting relatively low productivity and/or low preservation due to dryer conditions. A weak increase in OM (TOC_{2016} , RC_{2016} and decreasing CPI_{2016}) and BSi_{2016} , mostly consisting of diatoms, indicate an increase in productivity with time, interpreted to be a result of progressively wetter conditions from 17,266 to 16,179 cal. BP. This interpretation is in agreement with suggestions of dry conditions during the LGM and progressively wetter during the deglaciation. The previous Sekhokong study made by Fitchett et al. (2016b) showed an abundance of facultative planktonic diatoms and sedges pollen indicating wet conditions with standing water from 16,450 to 16,350 cal. BP. The low C/N_{2016} values (11 to 15) in combination with the highly negative $\delta^{13}\text{C}_{2016}$ values (-28‰), indicate a mixture of lacustrine algae and terrestrial C_3 plants (Figure 6 and 14 based on (Meyers, 2003)), which is generally the case throughout the whole sequence. These depleted $\delta^{13}\text{C}$ values indicates that no C_4 plants have been present at Sekhokong Mountain Range during the span of this study. Changes in C/N ratio may also reflect changes in degradation due to preferential loss of carbon during the breakdown of OM (Kaal et al., 2014).

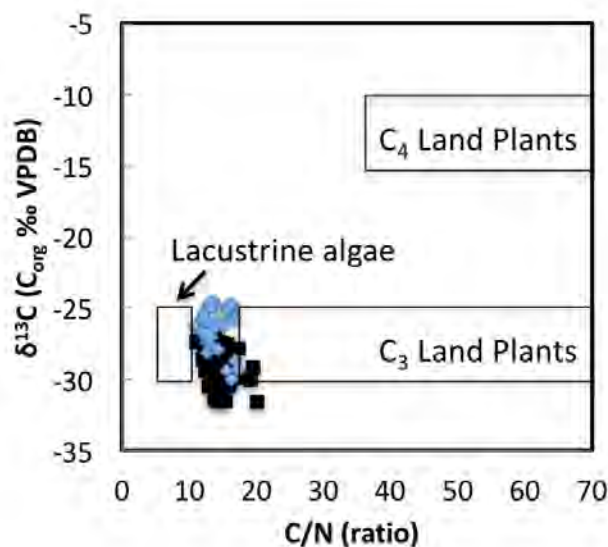


Figure 14. C/N ratio plotted against the $\delta^{13}\text{C}$ value can indicate the origin of the organic matter. The areas representing various organic matter is based on Meyers (2003). The black squares represent the SEK2014 and the blue diamonds represent the SEK2016 samples

6.3.2. SEK2016 Unit C: 16,115 to 15,315 cal. BP

This period has very low OM content (TOC_{2016} , RC2_{2016} and CPI_{2016}) and low abundance of BSi (RC4_{2016} and Si/Ti_{2016}) indicating relatively dry conditions, with low productivity and/or low preservation. High IM signals, as seen in both the RC1_{2016} and CPI_{2016} , are a consequence of low OM accumulation and the increased influence of detrital input from the catchment. There is a layer of coarser grain size (sand) identified by visual core description in the beginning of Unit C, which likely corresponds to the signals in the geochemical proxies. This could be due to drier conditions and a decrease in vegetation binding the soil, which may increase erosion (Kossler et al., 2011). Material that was formally stabilised by vegetation can, after a decrease in vegetation cover, be eroded without changes in transport energy. The low C/N_{2016} ratio seen in the main part of Unit C, interpreted to be a period of relatively dry climate conditions, can be explained by an increase in the roll of algal contribution relative to terrestrial vegetation (Meyers and Lallier-Vergès, 1999). Increased algal production can generally be seen during wet climate conditions as a result of increased nutrient supply due to run-off. However, such a productivity increase should then be recorded in the sediment together with elevated accumulation of OM content (Meyers and Lallier-Vergès, 1999), which is not the case in Unit C.

6.3.3. SEK2016 Unit B: 15,315 to 14,175 cal. BP

Unit B has the highest OM (TOC_{2016} and CPI_{2016} and CPI_{2016}) within the sediment sequence (including SEK2014) and low IM (RC1_{2016} and CPI_{2016}). There is a significant increase in BSi, identified by RC4_{2016} and the Si/Ti_{2016} ratio in the beginning of Unit B, just when the OM content starts to increase (TOC_{2016} , RC2_{2016} and CPI_{2016}) and the IM content decreases (RC1_{2016} and CPI_{2016}). Such rapid increases in BSi have previously been recognised after periods of dry climate conditions, as suggested in this study. During drier periods BSi, in the form of phytoliths, can accumulate in the watershed due to low surface runoff and fluvial transportation energy (Johnson et al., 2011). When the hydrological conditions shift and become more humid, an enhanced nutrient input and dissolved silica from the accumulated phytoliths would allow higher diatom production than normal. This could explain the increase in BSi, where diatoms make up the largest fraction, seen during the transition from dry conditions in Unit C to more humid conditions in Unit B. The C/N_{2016} ratio in combination with the $\delta^{13}\text{C}_{2016}$ values indicate a mixture of lacustrine algae and terrestrial C_3 plants, with an increasing influence of terrestrial input with time. The largest increase in C/N_{2016} values coincides with a slight decrease in OM, suggesting stronger influence of terrestrial OM in combination with lower productivity and/or preservation of OM, inferring a reduction in moisture.

6.3.4. SEK2016 Unit A: 14,175 to 13,440 cal. BP

Unit A has decreasing OM accumulation (TOC_{2016} , RC2_{2016} and CP1_{2016}) and higher influence of IM (CP1_{2016}), such as clay minerals (RC1_{2016}), siderite (RC3_{2016}) and goethite (RC5_{2016}), showing a fluctuating pattern. A decrease in OM would suggest drier conditions, resulting in reduced productivity and enhanced degradation leading to a net loss in preservation. Alternating layers of siderite and goethite, which sometimes coexist, indicate variations in redox conditions possibly as a consequence of fluctuations in the water table level and the access to OM for degradation. Relatively high water tables occurring under moister conditions, also resulting in higher productivity, would favour siderite precipitation. Relatively low water tables would occur under drier conditions with lower productivity, resulting in potentially higher O_2 levels in the water and sediment, promoting goethite precipitation and/or siderite alteration forming goethite.

The three main peaks of BSi (RC4_{2016} and Si/Ti_{2016}) in Unit A had low diatom contents and showed a high abundance of phytoliths with a parallelepiped elongated long morphology, identified as grass phytoliths. These parallelepiped elongated forms are specific for grasses (Poaceae), but non diagnostic for the subfamilies (Bamford et al., 2006; Mulholland and Rapp, 1992; Twiss et al., 1969). The phytoliths appear in the sediment stratigraphy right before siderite layers. As mentioned before, accumulation of phytoliths in the watershed have been seen during drier conditions due to limited runoff. When the hydrology changes, these accumulated phytoliths would be transported to the deposit. Dissolution of smaller phytoliths may explain the large proportion of elongated phytoliths (Twiss et al., 1969). The C/N_{2016} ratio in combination with the $\delta^{13}\text{C}_{2016}$ values indicate a mixture of lacustrine algae and terrestrial C_3 plants, with an C/N increase suggesting greater terrestrial influence due to drier conditions at 14,000 cal. BP.

The repetitive stratigraphic changes between BSi rich layers to siderite rich layers to goethite rich layers may reveal a geochemical signal of rapid hydrological variations during the Pleistocene/Holocene transition. The enhanced input of BSi, predominantly consisting of grass phytoliths, is interpreted as a change in transportation when going from drier to moister conditions. Increased moisture would result in higher water tables as well as increased productivity, creating conditions favouring siderite precipitation. As the climatic conditions become drier and the water table sinks, increased O_2 levels prevent the formation of siderite and instead favour goethite formation (alternatively alteration of siderite to goethite).

6.3.5. SEK2014 Unit 1: 13,280 cal. BP to present

Relatively low OM (TOC_{2014} , RC2_{2014} and CP1_{2014}) and high IM (RC1_{2014} and CP1_{2014}) is seen in the entire Unit 1. In the first half of Unit 1 (13,280 to 8,560 cal. BP) there is slightly increased OM that co-occurs with increased BSi (RC4_{2014} and Si/Ti_{2014}) as a consequence of higher net preservation of OM. Since the resolution is very poor in this part of the sequence it is hard to say if this is a signal from continuous environmental conditions or peaks from a more dynamic climatic period. Unfortunately, no microscopic evaluation of the BSi was done on the SEK2014 samples. However, since the increase in BSi co-occurs with the increase in OM and decrease in C/N , it likely indicates wetter conditions with higher productivity. The

elevated BSi signal would in this case represent increased abundance of diatoms as a result of higher water tables, which is supported by low C/N values as result of higher influence of lacustrine algae (Meyers and Lallier-Vergès, 1999). After this relatively wet period, a rapid change occurs at 8,560 cal. BP, where low OM and increased C/N ratios indicate low production and/or preservation of OM (TOC_{2014} , $RC2_{2014}$ and $CP1_{2014}$) with a higher influence of terrestrial plants, suggesting weaker wetland conditions due to a drying of the system until 6,970 cal. BP.

After 6,970 cal. BP, a small increase in OM (TOC_{2014} , $RC2_{2014}$ and $CP1_{2014}$) together with a significant increase in the BSi ($RC4_{2014}$ and Si/Ti_{2014}) proxies, suggests wetter conditions. A period of slightly decreasing OM and BSi follows, reaching the lowest values at 5,520 cal. BP, indicating a decrease in moisture. Thereafter the OM and BSi is increase again and the geochemical pattern suggests a period of wetter conditions, which peaks at approximately 3,400 cal. BP. At this time, a relatively big drop can be seen in the C/N values, reaching the lowest values of the whole sequence. These low C/N values >11 , together with $\delta^{13}C_{2014}$ values between -28% to -25% indicate that most of the OM originates from lacustrine algae, indicating moist condition and a relatively high water table.

After this wet period (5,520 to 3,400 cal. BP) it gets drier, indicated by a sharp decrease in OM (TOC_{2014} , $RC2_{2014}$ and $CP1_{2014}$) and BSi ($RC4_{2014}$ and Si/Ti_{2014}) at 3,320 cal. BP. Soon after, there are two peaks at 3,310 cal. BP and 3,280 cal. BP seen in $CP1_{2014}$, which indicates an increase of IM. Since this signal is not seen in the $RC1_{2014}$ data, also indicating IM but restricted to clay, it could be due to an input of a larger grain size fraction. This would be supported by the grain size analysis made by Fitchett et al. (2016b), which shows a significant increase in sand and a minor increase in gravel in these specific samples. There is a peak in the BSi, which together with the allochthonous $CP1_{2014}$ signal and low OM suggest an increase in transportation from the watershed. As mentioned before, no microscopic evaluation of the BSi content has been made, but since the other proxy signals are interpreted as allochthonous it suggests that the BSi is predominantly made up of terrestrial phytoliths. An increase in the C/N_{2014} ratio also indicates a stronger terrestrial influence. Fluvial transportation processes, rather than eolian, are suggested due to the large grain size and transport energy needed. It is difficult to say if these IM peaks are formed under a longer period with increased precipitation, or as short events. However, the sand and gravel indicate high-intensity runoff events under relatively dry conditions inferred by low OM, which would increase the erosion due to low vegetation cover (Marker, 1994). A dry and vegetation-poor watershed has a low capacity to take up water and is more sensitive to erosion (Kossler et al., 2011). This interpretation is only speculative and no conclusions can be made. Further investigation and higher resolution data would be needed to better understand these signals, duration and processes involved.

A transitional increase in moisture can be seen by an increase of OM (TOC_{2014} , RC2_{2014} and CP1_{2014}) and BSi (RC4_{2014} and Si/Ti_{2014}) after the proposed dry period that lasted until 3,190 cal. BP. The C/N_{2014} values are at first decreasing, indicating a stronger influence from lacustrine algae, but the terrestrial influence slightly increases with time, reaching C/N ratios around 13. The OM and BSi content peaks at 1,320 cal. BP before they decrease, which suggests a drying of the system. Due to low and varying resolution along the SEK2014 sequence the interpretation of Unit 1 is based on very few data points and should be taken with caution.

6.4 Regional context and implication of forcing mechanisms

When comparing different environmental reconstructions it is important to consider that (i) proxies differ in their rate of response to different forcings (Finné et al., 2010); (ii) different records have various resolution that are based on continuous vs discrete samples; and (iii) age models differ in their resolution and quality (Fitchett et al., 2016a). While the age-model for this study has good resolution between age dates (11-30 cm between samples), the age date acquired for the deepest sample was unacceptably young. The fact that the sample was obtained from the lowermost part of the core as well as the very low TOC content (1.5%) for this specific sample (SEKC233) increased the risk of contamination (Björck and Wohlfarth, 2001). This date was therefore excluded from the age-depth model, which does not show any reversals indicating continuous deposition. No abrupt boundaries could be identified in the stratigraphy, which supports the existence of continuous deposition.

Figure 15 shows environmental interpretations from four studies made in the Lesotho Highlands, where A-C are all from the Sekhokong Mountain Range and D from Mafadi wetland (see Figure 1A and 1B). Figure 15 also present the past variations in insolation intensity at 30° S (Berger and Loutre, 1991) (E) as well as $\delta^{18}\text{O}$ records (used as a temperature proxy) from two Antarctic ice cores: (F) the EPICA Dome C (Jouzel et al., 2001) and (G) Taylor Dome (Grootes et al., 2001; Steig et al., 2000). SST records from two marine sediment cores; (H) GeoB9307-3 with SSTs derived from lipid TEX^{86} values (Schefuß et al., 2011) and (I) MD79-257 with SSTs derived using U^k_{37} values from unsaturated C_{37} alkenones (Bard et al., 1997; Sonzogni et al., 1998) are also presented in Figure 15. The hydroclimatic reconstruction from the geochemical proxies will first be compared with the other records from the region to identify agreement within the different proxy datasets. The local climate response will then be put into a larger context, by comparing with records from more remote locations in the southern hemisphere, to identify possible relations to shifts in major climate systems.

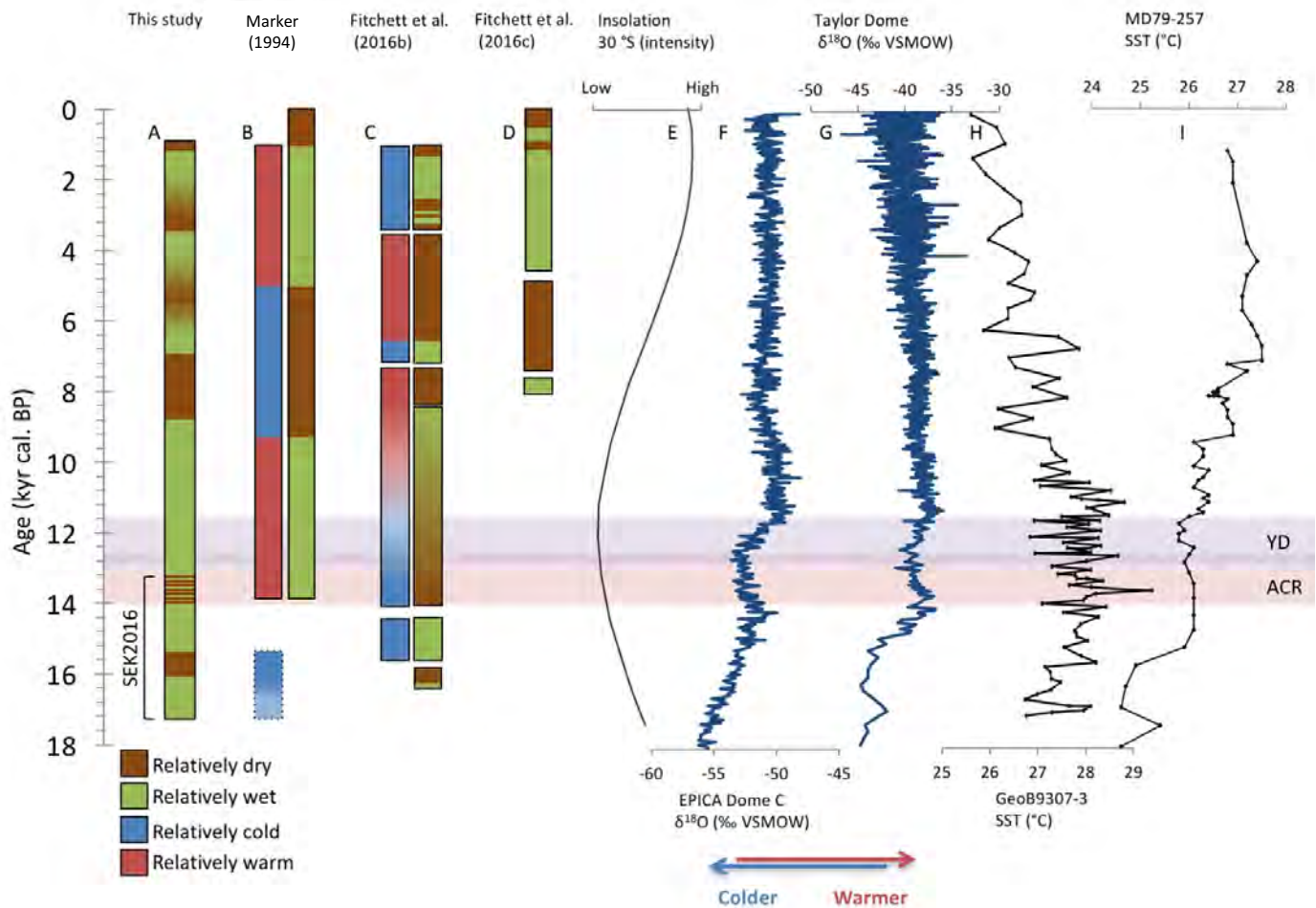


Figure 15 gives an overview of environmental reconstructions (relatively wet/dry and/or relatively warm/cold) from four studies in the Lesotho Highlands. (A) Paleohydrological variations in the Sekhokong Mountain Range based on the organic and inorganic geochemical proxies presented in this thesis. (B) Paleohydrological and paleotemperature variations in the Sekhokong Mountain Range based on stratigraphic and sedimentological proxies (Marker, 1994). The dashed lines marks undated sections. (C) Paleohydrological and paleotemperature variations in the Sekhokong Mountain Range based on fossil pollen and diatom data (Fitchett et al., 2016b). (D) Paleohydrological variations in the Mafadi Wetland based on fossil pollen and diatom data (Fitchett et al., 2016c). (E) Insolation intensity at 30° S based on insolation precession values (Berger and Loutre, 1991) (F) Antarctic ice core $\delta^{18}\text{O}$ values from EPICA Dome C (Jouzel et al., 2001). (G) Antarctic ice core $\delta^{18}\text{O}$ values from Taylor Dome (Grootes et al., 2001; Steig et al., 2000). (H) Sea surface temperature variations in the southwest Indian Ocean based on TEX86-derived SST record from GeoB9307-3 (Schefuß et al., 2011). (I) Sea surface temperature variations in the southwest Indian Ocean based on unsaturated C37 alkenones derived SST record from MD79-257 (Bard et al., 1997; Sonzogni et al., 1998). ACR = Antarctica Cold Reversal, YD = Younger Dryas.

The interpretation of the geochemical proxy data from this study starts with wet conditions at 17,335 cal. BP until a drier period occurs from 16,115 to 16,315 cal. BP, which is in line with the pollen and diatom data suggesting dry conditions from 16,450 to 15,870 cal. BP by Fitchett et al. (2016b). The onset and termination of this drier event occurs earlier based on pollen and diatom profiles as compared to the geochemical proxies, which could be an artefact of the lower sample resolution of the pollen and diatom data in this part of the sequence. These transitions may also be captured by the sedimentological proxies used by Marker (1994) that suggests a relative decrease in temperature before an increase at 13,500 cal. BP. Unfortunately, no age dates are available for this part of their reconstruction so whether these signals correspond to the same event or not is at this point only speculative.

A relatively wet period lasting from 15,315 until 14,175 cal. BP is seen in the geochemical proxies and in the diatom and pollen data by Fitchett et al. (2016b). After this period, the geochemical proxy data suggests variable hydrological fluctuations inferred by alternation of BSi, siderite and goethite until 13,440 cal. BP. The Sekhokong diatom and pollen data indicate a gradual transition from drier to wetter conditions after 14,175 to 8,560 cal. BP. The stratigraphic data by Marker (1994) indicates relatively warm and wet conditions from 13,500 to 9,500 cal. BP. The variable hydrological fluctuations inferred by the geochemical data strengthens interpretations made in previous studies by Smith et al. (2002) and Roberts et al. (2013) based on stable isotope data from archaeological sites in Lesotho (Figure 1B), which suggest an unstable regional climate during the Pleistocene-Holocene transition. These rapid variations were not captured in Fitchett et al. (2016b) nor by Marker (1994), possibly due to the low resolution of these records, which highlights the important advantage of the continuous, high-resolution dataset acquired in this study.

From 13,280 cal. BP, the geochemical data at Sekhokong changes from continuous high-resolution samples to discrete samples with lower resolution. During the period from 13,280 to 8,560 cal. BP the geochemical proxies suggest relatively wet conditions, with a slight increase in OM and BSi. During this period, no link could be made to the northern hemisphere YD cold event (12,900 to 11,600 cal. BP), which may be due to that this event occurs outside the range of the high-resolution data set. Previous studies from the relatively nearby Braamhoek record as well as Cango Cave to the south and Wonderkrater and Cold Air Cave to the north have identified local climatic response suggested to correspond to YD, which all infer drier conditions during this period (Norström et al., 2014, 2009; Talma and Vogel, 1992; Truc et al., 2013; Holmgren et al., 2003).

After 8,560 cal. BP, the geochemical proxies reveal low OM and BSi content as well as increased C/N values indicating that a drier period begins. This period of drier conditions last until 6,970 cal. BP. The Sekhokong pollen and diatom data also indicate a dry period, roughly during the same time, between 8,560 to 6,970 cal. BP (Fitchett et al., 2016b). Likewise, the stratigraphic data by Marker (1994) also indicates dry conditions during this period, but with an earlier start at 9,500 cal. BP and longer duration until 5,000 cal. BP. Again, this could be due to low sampling and age model resolution in Marker (1994). The pollen and diatom data from Mafadi wetland suggests relatively wet conditions from 8,140 cal. BP that changes to

drier conditions after 7,520 cal. BP, with a later onset of drier conditions compared to the geochemical proxies at Sekhokong (Fitchett et al., 2016c).

The geochemical proxies suggest a return to wetter conditions at 6,970 cal. BP until 940 cal. BP, which is the last sample in the record. This wetter period was interrupted by several drier periods at 5,520 cal. BP, 3,320 cal. BP and 1,200 cal. BP. The pollen and diatom data from Fitchett et al. (2016b) shows a similar pattern as the geochemical proxy data, with several changes between relatively wet and relatively dry conditions after 6,970 cal. BP. Although these fluctuations vary in duration compared to the interpretation based on the geochemical data, they occur roughly at the same time. The stratigraphic data by Marker (1994) does not show these variations. Instead they suggest persistent wetter conditions from 5,000 cal. BP to 1,000 cal. BP when drier conditions begin. As mentioned before, the low resolution of the Marker (1994) dataset might prevent detection of rapid climate variations with shorter duration.

The interpretation of the geochemical proxy data from Sekhokong shows a rough agreement to the local records presented as well as to the Mafadi record. Major shifts seen in the geochemical data can also be identified in the other records, which strengthens the idea that these changes would be representative for local and possibly regional hydroclimatic variations. There are some conflicts in the interpreted records, where differences in onset, termination and duration can be seen between studies. However, this is a common problem when comparing records with various resolution (Fitchett et al., 2016a). Also, the offset seen between the geochemical data and the pollen and diatom data, both from Sekhokong and Mafadi wetland, could be due differences in response and response time between the biological proxies and the geochemical proxies (Kylander et al., 2011).

Comparisons between the local hydrological shifts identified by geochemical proxies in Sekhokong and other records from the southern hemisphere could help to reveal important information about climate forcing mechanism and largescale migration of atmospheric circulation systems that control the hydrological shifts seen within the record. The climate shifts identified at Sekhokong in this study are rapid and mostly decennial to millennial in duration. The cyclic variation in insolation intensity is believed to be a major climate forcing mechanism (Berger, 1978; Laskar et al., 2004). Figure 15I shows the relative precessional insolation intensity at 30 °S, with low values during YD and early Holocene. These insolation variations influence atmospheric circulation and are believed to be a driving mechanism behind changes in precipitation patterns on multi-millennial timeframes in southern Africa (Norström et al., 2009). Given the temporal duration of the changes identified here, it would appear that changes in insolation are not the only forcing mechanism responsible for the observed paleohydrological variability.

The dry periods identified at the Sekhokong Mountain Range date to 16,115 to 15,315 cal. BP; 14,175 to 13,440 cal. BP; and 8,560 to 6,970 cal. BP and co-occur with lower $\delta^{18}\text{O}$ values seen in the Antarctic ice core records such as the EPICA Dome C and Taylor Dome records (Figure 15F and 15G) (Grootes et al., 2001; Jouzel et al., 2001; Steig et al., 2000).

These $\delta^{18}\text{O}$ ice records show a general warming trend during deglaciation with an interruption after 14,000 cal. BP that lasts until 12,500 cal. BP, which is defined as ACR and can be seen in most Antarctic ice cores (Grootes et al., 2001; Jouzel et al., 2001; Steig et al., 2000). The Taylor Dome ice core record shows greater $\delta^{18}\text{O}$ fluctuations between 20,000 and 15,000 cal. BP, rather than the gradual warming seen in EPICA Dome C and in other Antarctic ice cores (Steig et al., 2000). The local hydrological response in Sekhokong, with drier conditions during colder periods and wetter conditions during warmer periods, agrees with the climate response seen in the Cold Cave stalagmites (Holmgren et al., 2003). Colder periods and increased Antarctic sea-ice is believed to influence atmospheric circulation, with a northward extension and intensification of the polar vortex (Holmgren et al., 2003) and an equatorward shift of the tropical climate system and a possible weakening of the easterlies (Norström et al., 2009). This results in an increased influence of the westerlies over southern Africa and a northeast extension of the WRZ, as the influence of moisture bearing easterlies is decreased (Holmgren et al., 2003; Norström et al., 2009). This leads to drier conditions in the SRZ. Thus the more arid periods observed at Sekhokong may be a local response to atmospheric circulation shifts forced by temperature declines in Antarctica.

SST reconstructions based on marine sediment core records from GeoB9307-3 and MD79-257, both located in the East Indian Ocean outside the coast of Mozambique, show different patterns of change (Figure 15H and 15I). Namely, the decreasing and increasing SSTs seen in GeoB9307-3 and MD79-257, respectively, during the Holocene. The reason for this discrepancy is not clear, possibly as a result of the use of different proxy methods (GeoB9307-3 based on TEX86 and MD79-257 used unsaturated C37 alkenones). However, the most significant change seen in the majority of the geochemical proxies from Sekhokong, interpreted to be a rapid change to wetter conditions after 15,315 cal. BP coincides with a rapid increase in the SSTs seen in both GeoB9307-3 and MD79-257. This strengthens the importance of SSTs in the Indian Ocean to moisture availability in southeastern Africa. In the Wondercrater study made by Truc et al. (2013) increased moisture was identified between 15,000 and 13,500 cal. BP. This rapid hydroclimatic change shows a strong correlation to increasing SST in the Indian Ocean. Baker et al. (2014) identified dry and cold events in Mfabeni at 7,100, 5,300 and 1,400 cal. BP where the co-occurrence with lower SSTs in the GeoB9307-3 and MD79-257 record were highlighted. These events may correspond to the dryer periods seen in Sekhokong identified by the geochemical proxies at 8,560 to 6,970, 5,520, and after 1,200 cal. BP. Higher SSTs in the Indian Ocean have also been suggested to be a pre-condition, rather than the major forcing of increased rain in southern Africa (Schefuß et al., 2011). In this study by Schefuß et al. (2011) the rising SSTs predated the increased rainfall predictions. Instead, increased moisture flux over southern Africa was proposed to be due to the southward migration of the ITCZ, possibly as a consequence of elevated SSTs in the Indian Ocean.

Based on comparisons between multiple records, mechanisms forcing the hydrological shifts seen in the geochemical proxy data from Sekhokong region have most likely varied over time. The drier periods identified during 16,115 to 15,315 cal. BP; 14,175 to 13,440 cal. BP; and 8,560 to 6,970 cal. BP appear to correspond to increased influence of the westerlies as the

polar vortex got stronger due to cooling of Antarctica. The rapid moisture increase seen at 15,315 cal. BP, as the start of a wet period lasting until 14,175, is more likely to be a local response to rising SSTs in the Indian Ocean. Further investigation of continuous high-resolution records, such as the SEK2016 sequence presented here, is required to be able to link local and regional climate response in southern Africa to the large-scale climate forcing and the controlling mechanisms.

7. Conclusions

By using a suite of geochemical proxies processes responsible for the geochemical signal in two overlapping sediment sequences from Sekhokong, Lesotho, could be identified and linked to hydrological variations from 17,335 cal. BP to present. Five units were identified showing relatively wet conditions from 17,335 to 16,115 cal. BP, drier conditions from 16,115 to 15,315 cal. BP, relatively wet conditions from 15,315 to 14,175 cal. BP, multiple hydrological fluctuations during 14,175 to 13,440 cal. BP and relatively wet conditions from 13,280 cal. BP to present, interrupted by four drier periods. These four dryer periods occurred at 8,560 to 6,970 cal. BP, 5,520 cal. BP, 3,320 cal. BP and after 1,200 cal. BP.

The insights gained from this study indicate a relative drying in the Lesotho Highlands during colder conditions in the southern Hemisphere. Probably as a consequence of a northward extension of the polar vortex and migration of the ITCZ, which strengthened the influence of the westerlies and changes the source of moisture from the east (Indian Ocean) to the west (Atlantic Ocean). During warmer periods, the hydrological conditions tend to be relatively wet. The most dominant moisture increase seen in the geochemical proxy data at 15,315 to 14,175 cal. BP co-occurs with an increasing trend seen in SST records from the Indian Ocean. This further supports the association between higher SSTs in the Indian Ocean and increased rainfall in southeastern Africa. Warmer conditions would also cause a southward movement of the ITCZ, which intensifies the influence of the easterlies and increases moisture transport over the southeastern African continent.

Robust climate predictions are central to sustainable development of southern Africa, not least in Lesotho as it is one of the most important water resources in the region. The data presented in this study implies wetter conditions in the eastern Lesotho Highlands as the ongoing global warming progress (Niang et al., 2014), which supports model-projections by Engelbrecht et al. (2009) showing increased precipitation in southeast Africa during the austral summer. However, more data is required to better understand and predict the forcing mechanisms behind these climatic systems, how they will interact and the regional response to possible variations.

Acknowledgments

First of all, I would like to thank my supervisor Dr. Malin Kylander for giving me the opportunity to work with this project. Malin has been very supportive and has given me important advice along the way. Thank you, Prof. Stefan Grab at the University of Witwatersrand, for taking very good care of us during our time in Lesotho and for valuable support and feedback. Dr. Jennifer Fitchett at University of Witwatersrand, thank you for sharing previous results from the Sekhokong site as well as providing me with the samples retrieved 2014.

I would like to thank Prof. Richard Bindler and Dr. Johan Rydberg at Umeå University for helping with the XRF analysis. Heike Sigemund for helping me with the C/N and stable C isotope analysis and Carina Johansson for helping me with the sample preparation, both at Stockholm University. I would also like to thank Prof. Antonio Martínez-Cortizas for giving me the chance to work beside him and his incredible team at the University of Santiago de Compostela: Prof. Teresa Taboada for helping with XRD interpretation, Dr. Joeri Kaal for helping with the molecular composition of the OM and Mohamed Traoré for helping with the FTIR-ATR.

Thank you, Doc. Jan Risberg for helping me with the extraction of siliceous microfossils. Dr. Nolwenn Callac, thank you, for being a part of the sampling team. I would also like to thank Frej Yngwe, Jenny Sjöström and Diana Carlsson for being supportive during this, sometimes stressful period.

Last, but not least, acknowledgements to the Bolin centre for Climate Research and Swedish Society for Anthropology and Geography (SSAG) for helping to finance my project.



References

- Akande, S.O., Mücke, A., 1993. Depositional environment and diagenesis of carbonates at the Mamu/Nkporo formation, anambra basin, Southern Nigeria. *J. African Earth Sci.* 17, 445–456. doi:10.1016/0899-5362(93)90003-9
- Baker, A., Pedentchouk, N., Routh, J., Roychoudhury, A.N., 2017. Climatic variability in Mfabeni peatlands (South Africa) since the late Pleistocene. *Quat. Sci. Rev.* 160, 57–66. doi:10.1016/j.quascirev.2017.02.009
- Baker, A., Routh, J., Blaauw, M., Roychoudhury, A.N., 2014. Geochemical records of palaeoenvironmental controls on peat forming processes in the Mfabeni peatland, Kwazulu Natal, South Africa since the Late Pleistocene. *Palaeogeogr. Palaeoclimatol. Palaeoecol.* 395, 95–106. doi:10.1016/j.palaeo.2013.12.019
- Bamford, M., Albert, R.M., Dan, C., 2006. Plio – Pleistocene macroplant fossil remains and phytoliths from Lowermost Bed II in the eastern palaeolake margin of Olduvai Gorge, Tanzania. *Quat. Int.* 148, 95–112. doi:10.1016/j.quaint.2005.11.027
- Bard, E., Rostek, F., Sonzogni, C., 1997. Interhemispheric synchrony of the last deglaciation inferred from alkenone palaeothermometry. *Nature* 385, 707–710. doi:10.1038/385707a0
- Berger, A., Loutre, M.F., 1991. Insolation values for the climate of the last 10 million years. *Quat. Sci. Rev.* 10, 297–317.
- Berger, A.L., 1978. Long-Term Variations of Daily Insolation and Quaternary Climatic Change. *J. Atmos. Sci.* 35, 2362–2367. doi:10.1175/1520-0469(1978)035
- Berner, E.K., Berner, R.A., 1996. *Global Environment: Water, Air, and Geochemical Cycles*. Prentice-Hall, Inc, Upper Saddle River, Ney Jersey.
- Bigham, J.M., Fitzpatrick, R.W., Schulze, D.G., 2002. Iron Oxides, in: Dixon, J.B., Schulze, D.G. (Eds.), *Soil Mineralogy with Environmental Applications*, SSSA Book Series 7. Soil Science Society of America, Madison, WI, pp. 323–366. doi:10.2136/sssabookser7.c10
- Björck, S., Wohlfarth, B., 2001. 14C Chronostratigraphic Techniques in Paleolimnology, in: Last, W.M., Smol, J.P. (Eds.), *Tracking Environmental Change Using Lake Sediments. Volume 1*. Kluwer Academic Publishers, Dordrecht, pp. 205–245.
- Blaauw, M., 2010. Methods and code for “classical” age-modelling of radiocarbon sequences. *Quat. Geochronol.* 5, 512–518. doi:10.1016/j.quageo.2010.01.002
- Boko, M., Niang, I., Nyong, A., Vogel, C., Githeko, A., Medany, M., Osman-Elasha, B., Tabo, R., Yanda, P., 2007. Africa ,Climate change 2007: Impacts, adaptation and vulnerability, in: Parry, M.L., Canziani, O.F., J, P.P., van der Linden, P.J., E, H.C. (Eds.), *Contribution of Working Group II to the Fourth Assessment Report of the Intergovernmental Panel on Climate Change*. Cambridge University Press, Cambridge UK, pp. 433–467. doi:10.2134/jeq2008.0015br
- Bond, G.C., Lotti, R., 1995. Iceberg discharges into the north atlantic on millennial time scales during the last glaciation. *Science.* 267, 1005–1010. doi:10.1126/science.267.5200.1005
- Boyle, J.F., 2001. Inorganic Geochemical Methods in Palaeolimnology, in: Last, W.M., Smol, J.P. (Eds.), *Tracking Environmental Change Using Lake Sediments. Volume 2: Physical and Geochemical Methods*. Kluwer Academic Publishers, Dordrecht, pp. 83–141.
- Chase, B.M., Boom, A., Carr, A.S., Carré, M., Chevalier, M., Meadows, M.E., Pedro, J.B.,

- Stager, J.C., Reimer, P.J., 2015. Evolving southwest African response to abrupt deglacial North Atlantic climate change events. *Quat. Sci. Rev.* 121, 132–136. doi:10.1016/j.quascirev.2015.05.023
- Chase, B.M., Meadows, M.E., 2007. Late Quaternary dynamics of southern Africa's winter rainfall zone. *Earth-Science Rev.* 84, 103–138. doi:10.1016/j.earscirev.2007.06.002
- Chevalier, M., Brewer, S., Chase, B.M., 2017. Qualitative assessment of PMIP3 rainfall simulations across the eastern African monsoon domains during the mid-Holocene and the Last Glacial Maximum. *Quat. Sci. Rev.* 156, 107–120. doi:10.1016/j.quascirev.2016.11.028
- Cocozza, C., Orazio, V.D., Miano, T.M., Shotykh, W., 2003. Characterization of solid and aqueous phases of a peat bog profile using molecular fluorescence spectroscopy, ESR and FT-IR, and comparison with physical properties. *Org. Geochem.* 34, 49–60. doi:10.1016/S0146-6380(02)00208-5
- Conley, D.J., 1998. An interlaboratory comparison for the measurement of biogenic silica in sediments. *Mar. Chem.* 63, 39–48.
- Davies, S.J., Lamb, H.F., Roberts, S.J., 2015. Micro-XRF core Scanning in Palaeolimnology: Recent Developments, in: Croudace, I.W., Rothwell, R.G. (Eds.), *Micro-XRF Studies of Sediment Cores: Applications of a Non-Destructive Tool for the Environmental Sciences*. Springer, pp. 189–226. doi:10.1007/978-94-017-9849-5
- Dill, H.G., Techmer, A., 2009. The geogene and anthropogenetic impact on the formation of per descensum vivianite-goethite-siderite mineralization in Mesozoic and Cenozoic siliciclastic sediments in SE Germany. *Sediment. Geol.* 217, 95–111. doi:10.1016/j.sedgeo.2009.03.014
- Doner, H.E., Grossl, P.R., 2002. Carbonates and Evaporites, in: Dixon, J.B., Schulze, D.G. (Eds.), *Soil Mineralogy with Environmental Applications*, SSSA Book Series 7. Soil Science Society of America, Madison, WI, pp. 199–228. doi:10.2136/sssabookser7.c6
- Engelbrecht, F.A., Mcgregor, J.L., Engelbrecht, C.J., 2009. Dynamics of the Conformal-Cubic Atmospheric Model projected climate-change signal over southern Africa. *Int. J. Climatol.* 29, 1013–1033. doi:10.1002/joc
- ESRI, USGS, NOAA, 2009. Terrain with labels [Digital media]. URL https://tiledbasemaps.arcgis.com/arcgis/rest/services/World_Terrain_Base/MapServer [Accessed 20 October 2017]
- Finch, J.M., Hill, T.R., 2008. A late Quaternary pollen sequence from Mfabeni Peatland, South Africa: Reconstructing forest history in Maputaland. *Quat. Res.* 70, 442–450. doi:10.1016/j.yqres.2008.07.003
- Finné, M., Norström, E., Risberg, J., Scott, L., 2010. Siliceous microfossils as late-Quaternary paleo-environmental indicators at Braamhoek wetland, South Africa. *The Holocene* 20, 748–760. doi:10.1177/0959683610362810
- Fitchett, J.M., Grab, S.W., Bamford, M.K., Mackay, A., 2016a. A multi-disciplinary review of late Quaternary palaeoclimates and environments for Lesotho. *S. Afr. J. Sci.* 112, 9 pages. doi:10.17159/sajs.2016/20160045
- Fitchett, J.M., Grab, S.W., Bamford, M.K., Mackay, A.W., 2016b. A multi-proxy analysis of late Quaternary palaeoenvironments, Sekhokong Range, eastern Lesotho. *J. Quat. Sci.* 31, 788–798. doi:10.1002/jqs.2902
- Fitchett, J.M., Mackay, A.W., Grab, S.W., Bamford, M.K., 2016c. Holocene climatic variability indicated by a multi-proxy record from southern Africa's highest wetland. *The Holocene* 1–13. doi:10.1177/0959683616670467
- Gasse, F., Battarbee, R.W., 2004. Introduction, in: Battarbee, R.W., Gasse, F., Stickley, C.E.

- (Eds.), *Past Climate Variability through Europe and Africa*. Springer, Dordrecht, pp. 1–6. doi:10.1007/978-1-4020-2121-3_1
- Gasse, F., Chalié, F., Vincens, A., Williams, M.A.J., Williamson, D., 2008. Climatic patterns in equatorial and southern Africa from 30,000 to 10,000 years ago reconstructed from terrestrial and near-shore proxy data. *Quat. Sci. Rev.* 27, 2316–2340. doi:10.1016/j.quascirev.2008.08.027
- Grab, S.W., 2002. Characteristics and palaeoenvironmental significance of relict sorted patterned ground, Drakensberg plateau, southern Africa. *Quat. Sci. Rev.* 21, 1729–1744. doi:10.1016/S0277-3791(01)00149-4
- Grab, S.W., 1999. Block and Debris Deposits in the High Drakensberg, Lesotho, Southern Africa: Implications for High Altitude Slope Processes. *Geogr. Ann. Ser. A Phys. Geogr.* 81, 1–16. doi:10.1111/j.0435-3676.1999.00045.x
- Grab, S.W., Deschamps, C.L., 2004. Geomorphological and Geoecological Controls and Processes Following Gully Development in Alpine Mires, Lesotho. *Arctic, Antarct. Alp. Res.* 36, 49–58.
- Grootes, P.M., Steig, E.J., Stuiver, M., Waddington, E.D., 2001. The Taylor Dome Antarctic 180 Record and Globally Synchronous Changes in Climate. *Quat. Res.* 56, 289–298.
- Grootes, P.M., Stuiver, M., White, J.W.C., Johnsen, S., Jouzel, J., 1993. Comparison of oxygen isotope records from the GISP2 and GRIP Greenland ice cores. *Nature* 366, 552–554. doi:10.1038/366552a0
- Hogg, A.G., Hua, Q., Blackwell, P.G., Niu, M., Buck, C.E., Guilderson, T.P., Heaton, T.J., Palmer, J.G., Reimer, P.J., Reimer, R.W., Turney, C.S.M., Zimmerman, S.R.H., 2013. SHCal13 Southern Hemisphere Calibration, 0–50,000 Years cal BP. *Radiocarbon* 55, 1889–1903. doi:10.2458/azu_js_rc.55.16783
- Holmgren, K., Lee-thorp, J.A., Cooper, G.R.J., Lundblad, K., Partridge, T.C., Scott, L., Sithaldeen, R., Talma, A.S., Tyson, P.D., 2003. Persistent millennial-scale climatic variability over the past 25,000 years in Southern Africa. *Quat. Sci. Rev.* 22, 2311–2326. doi:10.1016/S0277-3791(03)00204-X
- Johnson, T.C., Brown, E.T., Shi, J., 2011. Biogenic silica deposition in Lake Malawi, East Africa over the past 150,000 years. *Palaeogeogr. Palaeoclimatol. Palaeoecol.* 303, 103–109. doi:10.1016/j.palaeo.2010.01.024
- Jouzel, J., Masson, V., Stenni, B., Petit, J.R., Schwander, J., Barkov, N.I., 2001. A new 27 kyr high resolution East Antarctic climate record. *geophy* 28, 3199–3202.
- Kaal, J., Schellekens, J., Nierop, K.G.J., Martínez Cortizas, A., Muller, J., 2014. Contribution of organic matter molecular proxies to interpretation of the last 55ka of the Lynch's Crater record (NE Australia). *Palaeogeogr. Palaeoclimatol. Palaeoecol.* 414, 20–31. doi:10.1016/j.palaeo.2014.07.040
- Kalbitz, K., Geyer, S., Geyer, W., 2000. A comparative characterization of dissolved organic matter by means of original aqueous samples and isolated humic substances. *Chemosphere* 40, 1305–1312. doi:10.1016/S0045-6535(99)00238-6
- Kossler, A., Tarasov, P., Scholaut, G., Nakagawa, T., Marshall, M., Brauer, A., Staff, R., Ramsey, C.B., Bryant, C., Lamb, H., Demske, D., Gotanda, K., Haraguchi, T., Yokoyama, Y., Yonenobu, H., Tada, R., 2011. Onset and termination of the late-glacial climate reversal in the high-resolution diatom and sedimentary records from the annually laminated SG06 core from Lake Suigetsu, Japan. *Palaeogeogr. Palaeoclimatol. Palaeoecol.* 306, 103–115. doi:10.1016/j.palaeo.2011.04.004
- Kylander, M.E., Ampel, L., Wohlfarth, B., Veres, D., 2011. High-resolution X-ray fluorescence core scanning analysis of Les Echets (France) sedimentary sequence : new insights from chemical proxies. *J. Quat. Sci.* 26, 109–117. doi:10.1002/jqs.1438

- Laskar, J., Robutel, P., Joutel, F., Gastineau, M., Correia, A.C.M., Levrard, B., 2004. Astrophysics A long-term numerical solution for the insolation. *Astronomy* 428, 261–285. doi:10.1051/0004-6361:20041335
- Levien, L., Prewitt, C.T., Weidner, D.J., Prewitt, C.T., Weidner, D.J., 1980. Structure and Elastic Properties of Quartz at Pressure. *Am. Mineral.* 65, 920–930.
- Marker, M.E., 1994. Sedimentary sequences at Sani Top, Lesotho highlands, southern Africa. *The Holocene* 4, 406–412.
- Meyer-Jacob, C., Vogel, H., Gebhardt, A.C., Wennrich, V., Melles, M., Rosen, P., 2014. Biogeochemical variability during the past 3.6 million years recorded by FTIR spectroscopy in the sediment record of Lake El'gygytgyn, Far East Russian Arctic. *Clim. Past* 10, 209–220. doi:10.5194/cp-10-209-2014
- Meyers, P.A., 2003. Application of organic geochemistry to paleolimnological reconstruction: a summary of examples from the Laurentian Great Lakes. *Org. Geochem.* 34, 261–289. doi:10.1016/S0146-6380(02)00168-7
- Meyers, P.A., Lallier-Vergès, E., 1999. Lacustrine sedimentary organic matter records of Late Quaternary paleoclimates. *J. Paleolimnol.* 345–372. doi:10.1023/A:1008073732192
- Meyers, P.A., Teranes, J.L., 2001. Sediment Organic Matter, in: Last, W.M., Smol, J.P. (Eds.), *Tracking Environmental Change Using Lake Sediments. Volume 2: Physical and Geochemical Methods.* Kluwer Academic Publishers, Dordrecht.
- Middleton, H. a., Nelson, C.S., 1996. Origin and timing of siderite and calcite concretions in late Palaeogene non- to marginal-marine facies of the Te Kuiti Group, New Zealand. *Sediment. Geol.* 103, 93–115. doi:10.1016/0037-0738(95)00092-5
- Monger, H.C., Kelly, E.F., 2002. Silica Minerals, in: Dixon, J.B., Schulze, D.G. (Eds.), *Soil Mineralogy with Environmental Applications*, SSSA Book Series 7. Soil Science Society of America, Madison, WI, pp. 611–636. doi:10.2136/sssabookser7.c20
- Montes-Hernandez, G., Pironon, J., 2009. Hematite and iron carbonate precipitation-coexistence at the iron – montmorillonite – salt solution – CO₂ interfaces ... *Appl. Clay Sci.* 45. doi:10.1016/j.clay.2009.06.004
- Mozley, P.S., Wersin, P., 1992. Geology Isotopic composition of siderite as an indicator of depositional environment Isotopie composition of siderite as an indicator of depositional environment. *Geology* 20, 817–820. doi:10.1130/0091-7613(1992)020<0817
- Mulholland, S.C., Rapp, G.J., 1992. A Morphological Classification of Grass Silica-Bodies, in: Rapp, G.J., Mulholland, S.C. (Eds.), *Phytolith Systematics: Emerging Issues.* Springer Science, New York.
- Müller, C.M., Pejčić, B., Esteban, L., Piane, C.D., Raven, M., Mizaikoff, B., 2014. Infrared attenuated total reflectance spectroscopy: an innovative strategy for analyzing mineral components in energy relevant systems. *Sci. Rep.* 4, 1–11. doi:10.1038/srep06764
- Nash, D.J., Grab, S.W., 2010. “A sky of brass and burning winds”: documentary evidence of rainfall variability in the Kingdom of Lesotho, Southern Africa, 1824-1900. *Clim. Change* 101, 617–653. doi:10.1007/s10584-009-9707-y
- Niang, I., Puppel, O.C., Abdrabo, M.A., Essel, A., Lennard, C., Padgham, J., Urquhart, P., 2014. Africa, in: Barros, V.R., Field, C.B., Dokken, D.J., Mastrandrea, M.D., Mach, K.J., Bilir, T.E., Chatterjee, M., Ebi, K.L., Eftrada, Y.O., Genova, R.C., Girma, B., Kissel, E.S., Levy, A.N., MacCracken, S., Mastrandrea, P.R., White, L.L. (Eds.), *Climate Change 2014: Impacts, Adaption and Vulnerability. Part B: Regional Aspects. Contribution of Working Group II to the Fifth Assessment Report of Intergovernmental Panel of*

- Climate Change. Cambridge University Press, Cambridge, United Kingdom and New York, NY, USA, pp. 1199–1265.
- Norström, E., Neumann, F.H., Scott, L., Smittenberg, R.H., Holmstrand, H., Lundqvist, S., Snowball, I., Sundqvist, H.S., Risberg, J., Bamford, M., 2014. Late Quaternary vegetation dynamics and hydro-climate in the Drakensberg, South Africa. *Quat. Sci. Rev.* 105, 48–65. doi:10.1016/j.quascirev.2014.09.016
- Norström, E., Scott, L., Partridge, T.C., Risberg, J., Holmgren, K., 2009. Reconstruction of environmental and climate changes at Braamhoek wetland, eastern escarpment South Africa, during the last 16,000 years with emphasis on the Pleistocene – Holocene transition. *Palaeogeogr. Palaeoclimatol. Palaeoecol.* 271, 240–258. doi:10.1016/j.palaeo.2008.10.018
- Olago, D.O., Odada, E.O., 2004. Palaeo-Research in Africa: Relevance to Sustainable Environmental Management and Significance for the Future, in: Battarbee, R.W., Gasse, F., Stickley, C.E. (Eds.), *Past Climate Variability through Europe and Africa*. Springer, Dordrecht, pp. 551–566.
- Oldfield, F., Thompson, R., 2004. Archives and Proxies Along the PRP III Transect, in: Battarbee, R.W., Gasse, F., Stickley, C.E. (Eds.), *Past Climate Variability through Europe and Africa*. Springer, Dordrecht, pp. 7–23. doi:10.1007/978-1-4020-2121-3_2
- Parker, A.G., Lee-Thorp, J., Mitchell, P.J., 2011. Late Holocene Neoglacial conditions from the Lesotho highlands, southern Africa: Phytolith and stable carbon isotope evidence from the archaeological site of Likoaeng. *Proc. Geol. Assoc.* 122, 201–211. doi:10.1016/j.pgeola.2010.09.005
- Partridge, T.C., Scott, L., Schneider, R.R., 2004. Between Agulhas and Benguela: Response of Southern African Climates of the Late Pleistocene to Current Fluxes, Orbital Precession and the Extent of the Circum-Atlantic Vortex, in: Battarbee, R.W., Gasse, F., Stickley, C.E. (Eds.), *Past Climate Variability through Europe and Africa*. Springer, Dordrecht, pp. 45–91. doi:10.1007/978-1-4020-2121-3_4
- Pedro, J.B., Ommen, T.D. Van, Rasmussen, S.O., Morgan, V.I., Chappellaz, J., Moy, A.D., 2011. The last deglaciation: timing the bipolar seesaw. *Clim. Past* 7, 671–683. doi:10.5194/cp-7-671-2011
- Pérez-Rodríguez, M., Horák-Terra, I., Rodríguez-Lado, L., Martínez Cortizas, A., 2016. Modelling mercury accumulation in minerogenic peat combining FTIR-ATR spectroscopy and partial least squares (PLS). *Spectrochim. Acta - Part A Mol. Biomol. Spectrosc.* 168, 65–72. doi:10.1016/j.saa.2016.05.052
- Ragueneau, O., Leynaert, A., Treguer, P., DeMaster, D.J., Anderson, R.F., 1996. Opal Studied as a Marker of Paleoproductivity. *Earth Sp. Sci. News* 77, 491–492.
- Reason, C.J.C., Landman, W., Tennant, W., 2006. Seasonal to Decadal Prediction of Southern African Climate and Its Links with Variability of the Atlantic Ocean. *Am. Meteorol. Soc.* 941–956. doi:10.1175/BAMS-87-7-941
- Renard, F., Putnis, C. V., Montes-Hernandez, G., King, H.E., 2017. Siderite dissolution coupled to iron oxyhydroxide precipitation in the presence of arsenic revealed by nanoscale imaging. *Chem. Geol.* 449, 123–134. doi:10.1016/j.chemgeo.2016.12.001
- Roberts, P., Lee-Thorp, J.A., Mitchell, P.J., Arthur, C., 2013. Stable carbon isotopic evidence for climate change across the late Pleistocene to early Holocene from Lesotho, southern Africa. *J. Quat. Sci.* 28, 360–369. doi:10.1002/jqs.2624
- Rout, K., Mohapatra, M., Anand, S., 2011. 2-line ferrihydrite: synthesis, characterization and its adsorption behaviour for removal of Pb(II), Cd(II), Cu(II) and Zn(II) from aqueous solutions. *Dalt. Trans.* 41, 3302–3312. doi:10.1039/c2dt11651k

- Rydberg, J., 2014. Wavelength dispersive X-ray fluorescence spectroscopy as a fast, non-destructive and cost-effective analytical method for determining the geochemical composition of small loose-powder sediment samples. *J. Paleolimnol.* 52, 265–276. doi:10.1007/s10933-014-9792-4
- Schefuß, E., Kuhlmann, H., Prange, M., Pätzold, J., 2011. Forcing of wet phases in southeast Africa over the past 17,000 years. *Nature* 480, 509–512. doi:10.1038/nature10685
- Scott, L., Lee-thorp, J.A., 2004. Holocene climatic trends and rythems in southern Africa, in: Battarbee, R.W., Gasse, F., Stickley, C.E. (Eds.), *Past Climate Variability through Europe and Africa*. Springer, Dordrecht, pp. 69–92. doi:10.1007/978-1-4020-2121-3_5
- Sene, K.J., Jones, D.A., Meigh, J.R., Farquharson, F.A.K., 1998. Rainfall and flow variations in the Lesotho Highlands. *Int. J. Climatol.* 18, 329–345. doi:10.1002/(SICI)1097-0088(19980315)18:3<329::AID-JOC251>3.0.CO;2-5
- Smith, B.N., Epstein, S., 1971. Two Categories of $^{13}\text{C}/^{12}\text{C}$ Ratios for Higher Plants. *Plant Physiol.* 47, 380–384.
- Smith, J.M., Lee-Thorp, J.A., Sealy, J.C., 2002. Stable carbon and oxygen isotopic evidence for late Pleistocene to middle Holocene climatic fluctuations in the interior of southern Africa. *J. Quat. Sci.* 17, 683–695. doi:10.1002/jqs.687
- Sonzogni, C., Bard, E., Rostek, F., 1998. Tropical sea-surface temperatures during the last glacial period: a view based on alkenones in Indian Ocean sediments. *Quat. Sci. Rev.* 17, 1185–1201.
- STATSSA, 2017. Statistical Release: Mid-year population estimates [PDF]. URL http://www.statssa.gov.za/?page_id=1854&PPN=P0302&SCH=7048 [Accessed 20 October 2017]
- Steig, E.J., Morse, D.L., Waddington, E.D., Stuiver, M., Pieter, M., Mayewski, P.A., Twickler, M.S., Whitlow, S.I., Steig, E.J., Morse, D.L., Waddington, E.D., Stuiver, M., Grootes, P.M., Mayewski, P.A., Twickler, M.S., Whitlow, S.I., 2000. Wisconsinan and Holocene Climate History from an Ice Core at Taylor Dome, Western Ross Embayment, Antarctica. *Geogr. Ann. Ser. A Phys. Geogr. A*, 213–235.
- Stone, A.E.C., 2014. Last Glacial Maximum conditions in southern Africa: Are we any closer to understanding the climate of this time period? *Prog. Phys. Geogr.* 38, 519–542. doi:10.1177/0309133314528943
- Swann, G.E.A., Patwardhan, S. V., 2011. Application of Fourier Transform Infrared Spectroscopy (FTIR) for assessing biogenic silica sample purity in geochemical analyses and palaeoenvironmental research. *Clim. Past* 7, 65–74. doi:10.5194/cp-7-65-2011
- Takano, Y., James, J., Kojima, H., Yokoyama, Y., Tanabe, Y., Sato, T., Ogawa, N.O., Ohkouchi, N., Fukui, M., 2012. Applied Geochemistry Holocene lake development and glacial-isostatic uplift at Lake Skallen and Lake Oyako, Lützow-Holm Bay, East Antarctica: Based on biogeochemical facies and molecular signatures. *Appl. Geochemistry* 27, 2546–2559. doi:10.1016/j.apgeochem.2012.08.009
- Talma, S.A., Vogel, J.C., 1992. Late Quaternary Paleotemperatures Derived from a Speleothem Cango Caves, Cape Province, South Africa. *Quat. Res.* 37, 203–213.
- Truc, L., Chevalier, M., Favier, C., Cheddadi, R., Meadows, M.E., Scott, L., Carr, A.S., Smith, G.F., Chase, B.M., 2013. Quantification of climate change for the last 20,000 years from Wonderkrater, South Africa: Implications for the long-term dynamics of the Intertropical Convergence Zone. *Palaeogeogr. Palaeoclimatol. Palaeoecol.* 386, 575–587. doi:10.1016/j.palaeo.2013.06.024

- Twiss, P.C., Suess, E., Smith, R.M., 1969. Morphological Classification of Grass Phytoliths. *Siol Sci. Soc. Am. Proc.* 33, 109–115.
- Tyson, P.D., Preston-Whyte, R.A., 2000. *The Weather and Climate of Southern Africa*. Oxford University Press Southern Africa, South Africa.
- USGS, 2017. ASTER GDEM [Digital elevation model]. URL <https://earthexplorer.usgs.gov> [Accessed 20 October 2017]
- Valsecchi, V., Chase, B.M., Slingsby, J.A., Carr, A.S., Quick, L.J., Meadows, M.E., Cheddadi, R., Reimer, P.J., 2013. A high resolution 15,600-year pollen and microcharcoal record from the Cederberg Mountains, South Africa. *Palaeogeogr. Palaeoclimatol. Palaeoecol.* 387, 6–16. doi:10.1016/j.palaeo.2013.07.009

Appendix A, Age-depth model

The setting used to do the age-depth model for SEK2016, using clam.R. Settings (square brackets give names of the constants)

Calibration curve: SHCal13.14C

Age-depth model: smooth spline [type=4] with spar = 0.3 [smooth]

Weighted by the calibrated probabilities [wghts=1]

Calculations at 95% confidence ranges [prob=0.95]

Amount of iterations: 1000 [its]

Calendar age point estimates for depths based on modes/maxima/intercepts of the dated levels [est=6]

Calendar scale used: cal BP [BCAD=FALSE] at a resolution of 1 yr [yrsteps]

Ages were calculated every 0.01 [every] cm [depth], from 315 [dmin] to 460 [dmax] cm

Dates assumed outlying [outliers]: 10 (Beta-466036)

Goodness-of-fit (-log, lower is better): 11.08

Any models with age-depth reversals were removed

Produced Tue Aug 15 16:11:19 2017

Appendix B, Linear regression models

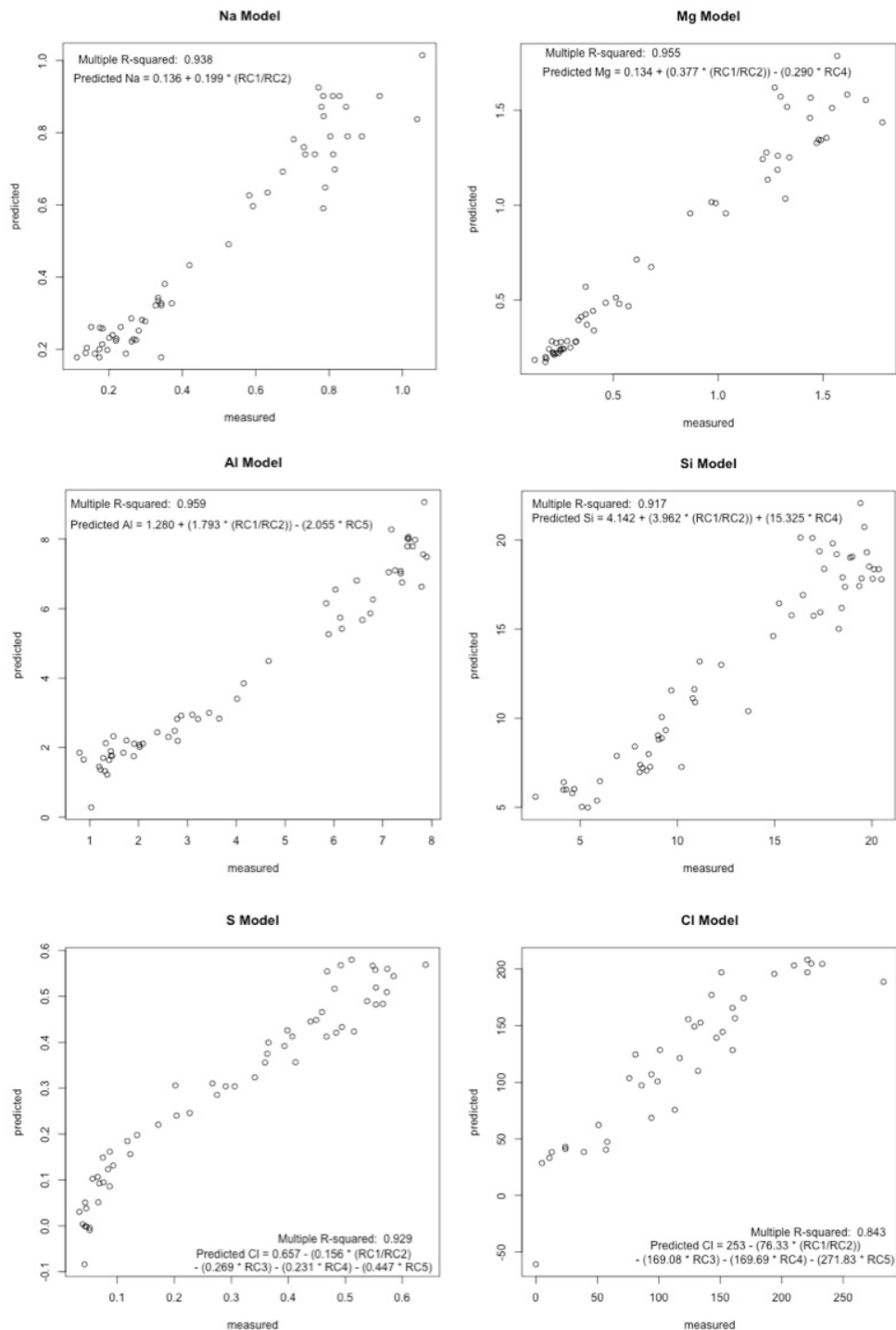


Figure B1. Models used for the linear regression (achieved in R statistical software) to predict missing values of Na, Mg, Al, Si, S and Cl.

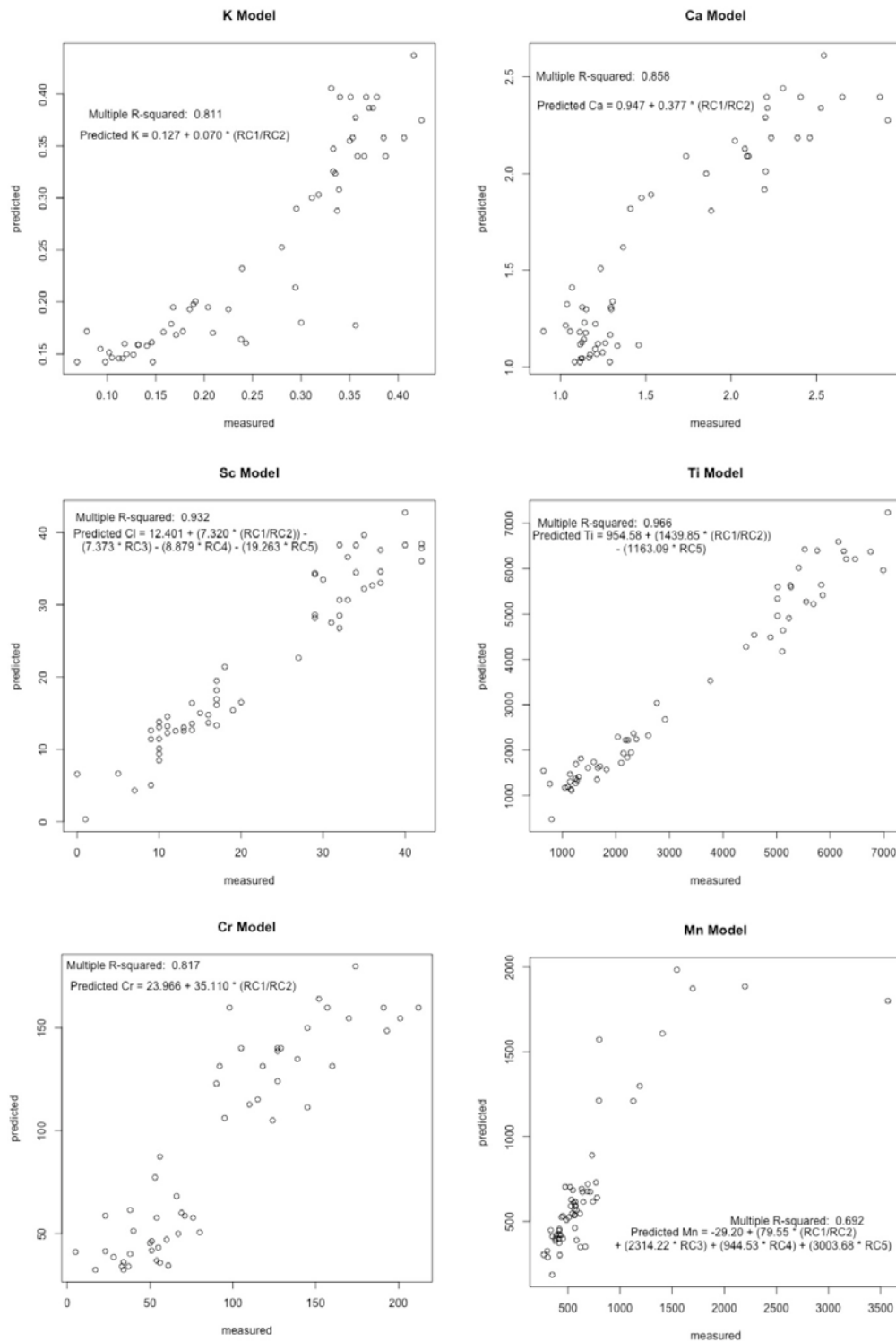


Figure B2. Models used for the linear regression (achieved in R statistical software) to predict missing values of K, Ca, Sc, Ti, Cr and Mn.

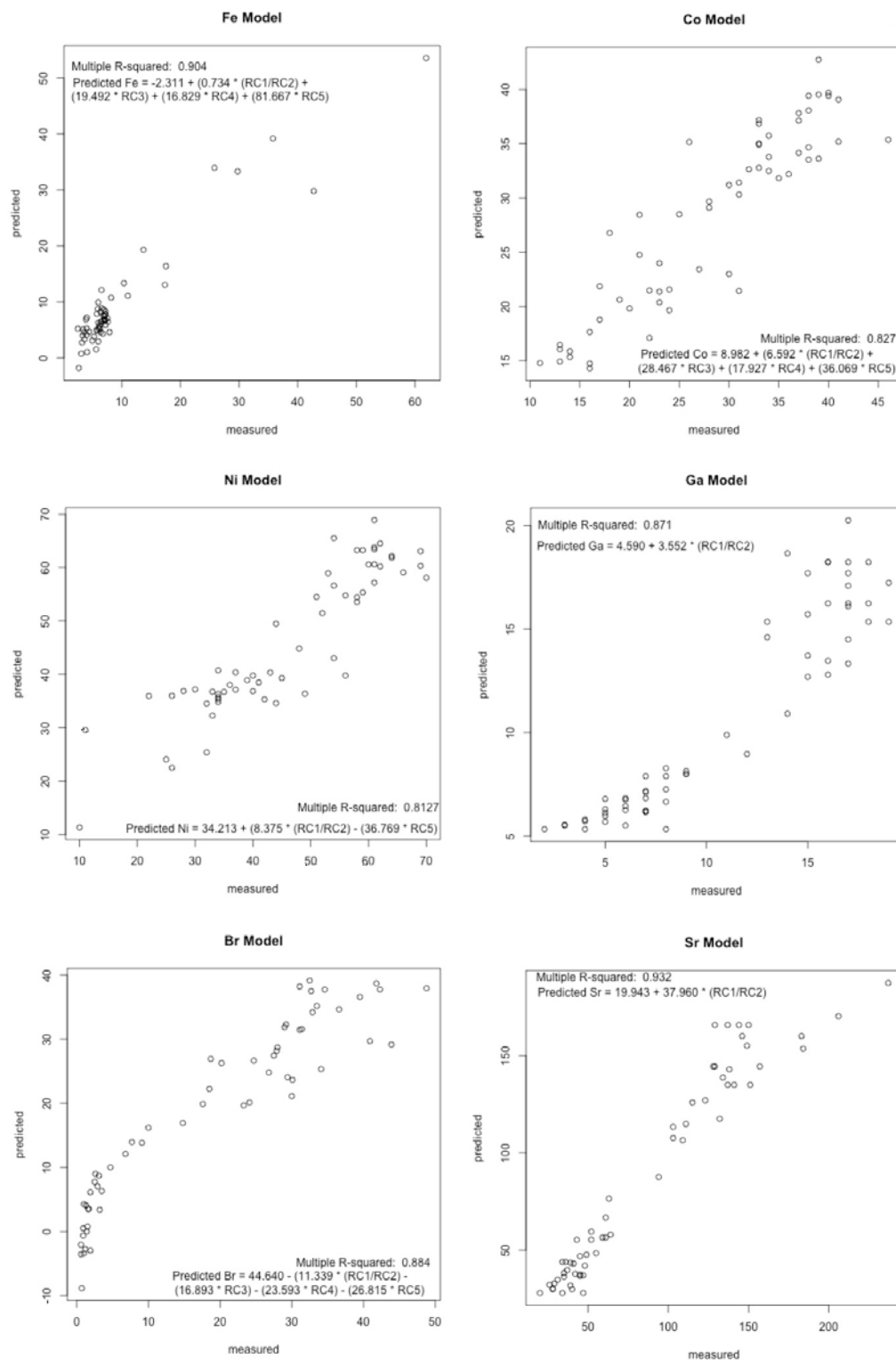


Figure B3. Models used for the linear regression (achieved in R statistical software) to predict missing values of Fe, Co, Ni, Ga, Br and Sr.

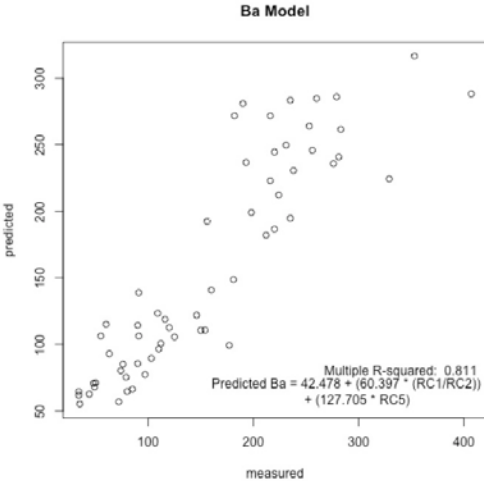


Figure B4. Model used for the linear regression (achieved in R statistical software) to predict missing values of Ba.

Appendix C, Conventional XRF

Appendix C. The precision was based on replicates, the highest standard deviation and relative standard deviation are presented. The accuracy was based on measurements of the CRM NCS DC-70314 standard, the highest difference and relative difference are presented. PCA loadings for both SEK2014 and SEK2016. The loadings for SEK2016 are based on the predicted values from the linear regression.

Element	XRF analysis quality				PCA loadings			
	Precision		Accuracy		SEK2014	SEK2016		
	SD	Rel. SD	Difference	Rel. difference	CP1	CP1	CP2	CP3
Na (%)	0.04	5.92	0.04	3.41	0.52	0.97	0.14	0.13
Mg (%)	0.07	5.08	0.05	9.59	0.44	0.95	0.18	0.17
Al (%)	0.19	3.80	0.13	2.24	0.95	0.8	0.21	0.12
Si (%)	0.56	3.13	0.96	2.61	0.91	0.88	0.1	0.06
P (PPM)	46.67	5.95	32.50	7.96	-0.27			
S (%)	0.01	15.71	0.00	25.33	-0.82	-0.86	0.33	-0.01
Cl (PPM)	21.92	76.91	52.50	77.78	-0.87	-0.96	0.17	-0.03
K (%)	0.01	4.66	0.08	3.96	0.93	0.9	0.22	0.2
Ca (%)	0.13	5.79	0.04	4.42	0.21	0.94	0.15	0.16
Sc (PPM)	2.12	12.86	2.25	24.32	0.90	0.89	0.35	0.22
Ti (PPM)	219.20	4.43	40.00	1.44	0.85	0.95	0.23	0.18
V (PPM)	50.20	5.75	2.50	4.67	0.30			
Cr (PPM)	47.38	34.46	7.75	27.43	0.73	0.93	0.2	0.12
Mn (PPM)	51.62	4.76	24.25	4.46	0.06	-0.12	-0.97	0.14
Fe (%)	0.42	5.29	0.12	5.70	0.12	-0.09	-0.87	-0.44
Co (PPM)	2.83	10.88	1.00	11.11	0.37	0.75	-0.56	0.26
Ni (PPM)	2.12	7.71	0.00	0.00	0.77	0.77	0.4	0.42
Cu (PPM)	4.24	6.24	5.25	28.77	0.18			
Zn (PPM)	3.54	3.95	1.50	2.80	0.73			
Ga (PPM)	1.41	35.36	0.75	5.66	0.95	0.93	0.14	0.14
Br (PPM)	2.19	22.33	0.13	8.20	-0.84	-0.94	0.14	0.02
Sr (PPM)	40.31	28.48	1.00	0.85	0.68	0.96	0.14	0.13
Ba (PPM)	128.69	44.38	1.00	0.29	0.58	0.95	0.02	0.03
C _{org} (%)					-0.83	-0.95	0.21	0.03
N (%)					-0.83	-0.95	0.19	0.06

Appendix D, XRD

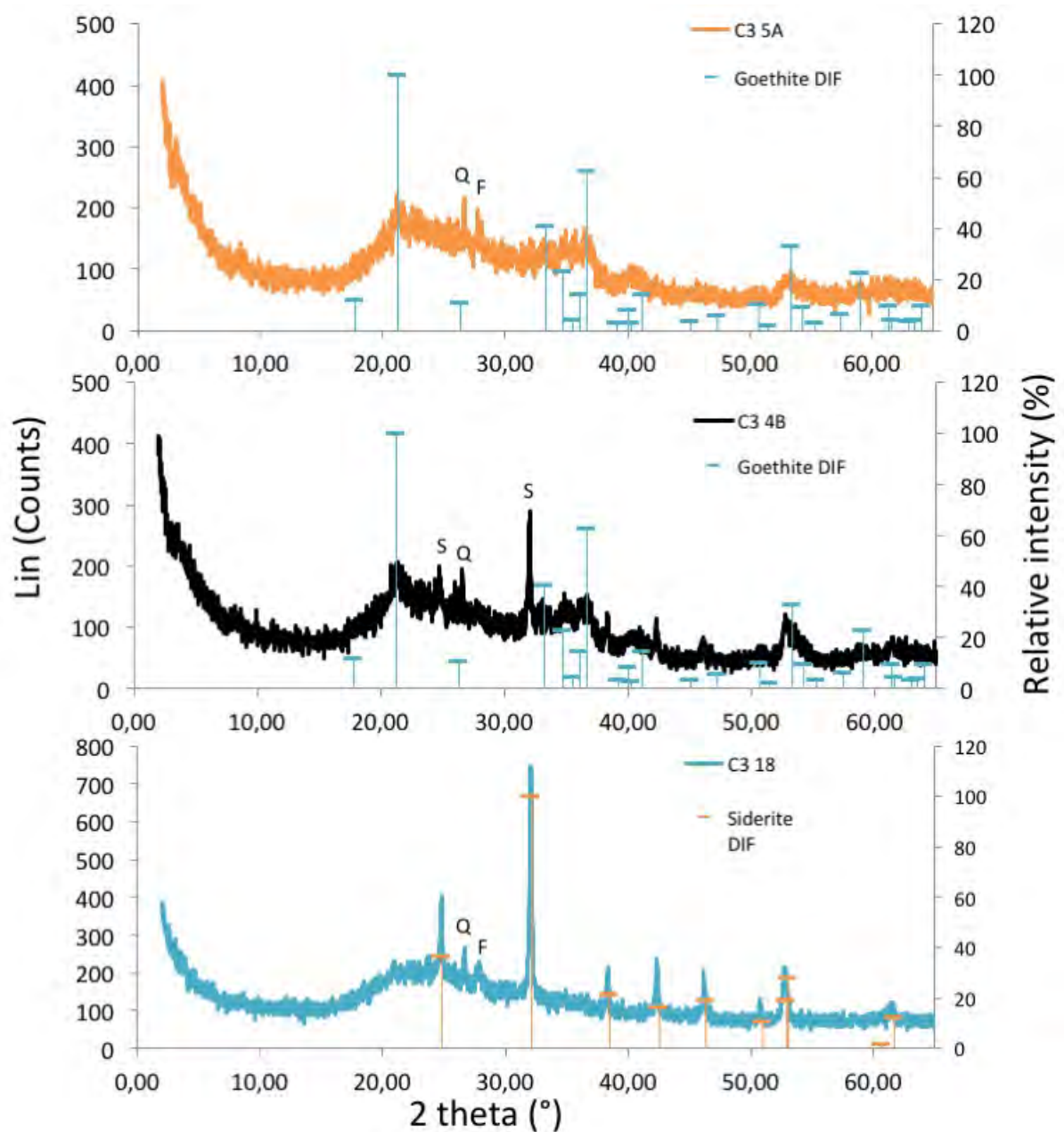


Figure D. Diffractograms for the XRD analysis made on SEK2016 C35A with an interpolated age-date of 13,635 cal. BP (top), SEK2016 C34B with an interpolated age-date of 13,610 cal. BP (middle) and SEK2016 C318 with an interpolated age-date of 14,000 cal. BP (bottom). A goethite reference sample is shown in the top and middle graph (Levien et al., 1980) and a siderite reference sample (Renard et al., 2017) is shown in the bottom graph. Q=quartz, F=feldspar and S=siderite are indicating other significant peaks identified in the diffractograms.



Stockholm
University

Master Thesis

Degree Project in
Marine Geology 60 hp

Hydroclimatic variations over the past ~17,400 years in the Lesotho Highlands, southern Africa: a geochemical proxy approach

Mikaela Holm



Stockholm 2017

Department of Geological Sciences
Stockholm University
SE-106 91 Stockholm